FISEVIER

Contents lists available at ScienceDirect

Journal of Molecular Spectroscopy

journal homepage: www.elsevier.com/locate/yjmsp





Diborane anharmonic vibrational frequencies and Intensities: Experiment and theory

Aaron I. Strom^a, Ibrahim Muddasser^a, Guntram Rauhut^b, David T. Anderson^{a,*}

- a Department of Chemistry, University of Wyoming, Laramie, WY 82071-3838, USA
- ^b University of Stuttgart, Institute for Theoretical Chemistry, Pfaffenwaldring 55, 70569 Stuttgart, Germany

ARTICLE INFO

Keywords: Matrix Isolation Spectroscopy Anharmonic Vibrational Dynamics Infrared Spectroscopy Computational Spectroscopy Diborane Fermi Resonance Darling-Dennison Resonance

ABSTRACT

The vibrational dynamics of diborane have been extensively studied both theoretically and experimentally ever since the bridge structure of diborane was established in the 1950s. Numerous infrared and several Raman spectroscopic studies have followed in the ensuing years at ever increasing levels of spectral resolution. In parallel, ab initio computations of the underlying potential energy surface have progressed as well as the methods to calculate the anharmonic vibration dynamics beyond the double harmonic approximation. Nevertheless, even 70 years after the bridge structure of diborane was established, there are still significant discrepancies between experiment and theory for the fundamental vibrational frequencies of diborane. In this work we use parahydrogen (pH₂) matrix isolation infrared spectroscopy to characterize six fundamental vibrations of B₂H₆ and B₂D₆ and compare them with results from configuration-selective vibrational configuration interaction theory. The calculated frequencies and intensities are in very good agreement with the pH₂ matrix isolation spectra, even several combination bands are well reproduced. We believe that the reason discrepancies have existed for so long is related to the large amount of anharmonicity that is associated with the bridge BH stretching modes. However, the calculated frequencies and intensities reported here for the vibrational modes of all three boron isotopologues of B₂H₆ and B₂D₆ are within \pm 2.00 cm⁻¹ and \pm 1.44 cm⁻¹, respectively, of the experimental frequencies and therefore a refined vibrational assignment of diborane has been achieved.

1. Introduction

Starting with its conception in the 1950s matrix isolation spectroscopy (MIS) has proven to be a powerful tool to characterize the vibrational spectrum of polyatomic molecules using direct infrared absorption spectroscopy [1-4]. MIS originated from the desire to spectroscopically characterize highly reactive species by trapping them in a chemically inert matrix host to build up sufficient concentrations of the guest species such that direct absorption (IR or UV) can be used to both identify the molecule (set of vibrational frequencies) and quantify its concentration (intensities). In the 1970s several computational chemistry packages were developed which allowed experimentalists for the first time to calculate from first principles the vibrational frequencies and intensities of a prospective small molecule at the harmonic level. This combination of MIS and ab initio software has proved invaluable in the assignment of new chemical species that form in matrix isolation experiments. However, if the difference between the calculated and observed vibrational frequencies is sufficiently large, this weakens

considerably the positive identification of new species [5,6]. Furthermore, some polyatomic molecules require going beyond the so-called double harmonic approximation [7], which treats the potential energy functions as second-order polynomials and the dipole moment functions as first-order polynomials, to simulate the infrared spectrum accurately enough to allow comparison with high-resolution infrared data.

Fast forward to 2024 and now to some extent MIS has been superseded by high resolution IR spectroscopy in supersonic expansions where the molecule (or cluster) is probed *in vacuo* [8]. A supersonic expansion cools the entrained molecule of interest thereby greatly simplifying the rovibrational spectrum by collapsing the rotational populations to just the lowest levels, and it makes direct-IR absorption more sensitive for the same reason. Nowadays the whole rovibrational spectrum can be simulated by *ab initio* methods [9,10] and compared with experiment to accomplish the same task of matching new molecules to their infrared spectra, where both experiment and theory treat the molecule in isolation. In contrast, MIS necessarily involves the guest–host intermolecular interactions which can lead to some

E-mail address: danderso@uwyo.edu (D.T. Anderson).

^{*} Corresponding author.

peculiarities in MIS that intricately depend on the properties of the specific guest-host combination [11]. Noble gases such as argon, krypton, and xenon as well as molecular nitrogen were first used as matrix hosts due to their weak intermolecular forces, transparency in the IR region, and relatively high melting points which meant they could be deposited and maintained at modest cryogenic temperatures with the available closed-cycle helium cryostats [11]. These guest-host intermolecular interactions lead to mode dependent matrix shifts ($\Delta \nu =$ $\nu_{\text{matrix}} - \nu_{\text{gas}}$) in the vibrational modes of the guest species, and thus comparing MIS results with computations of the isolated molecule requires accounting for these matrix shifts. Jacox [12,13] compiled the matrix shifts of 230 diatomic molecules isolated in noble gas and nitrogen matrices and found that the matrix shifts in solid argon are typically smaller than 2 %, and that the matrix shifts increase in the order Ne < Ar < Kr < Xe < N₂. Today with advances in cryogenics, researchers are now increasingly using neon (Ne) and parahydrogen (pH₂) as matrix hosts, opening new possibilities as will be discussed in this work.

Our experimental group exclusively utilizes solid pH₂ as a matrix host for a variety of problems in chemical physics, and in this work, we investigate the anharmonic vibrational spectrum of a stable small molecule for comparison with configuration-selective vibrational configuration interaction (VCI) calculations that go beyond the double harmonic approximation and intrinsically treat all kinds of resonances, e.g., Fermi or Darling-Dennison anharmonic resonances [14-17]. Many of the advantages that MIS has for the characterization of transient species carry over to detailed vibrational studies of stable molecules; broad spectral coverage allows all the infrared active vibrations of a guest species in a specific spectral region to be probed at high resolution to produce precise vibrational peak frequencies and absorption intensities for an isolated guest species at low concentration. One important advantage that the pH2 host affords over noble gas matrix hosts is the superior optical quality that can be achieved in rapid vapor deposited pH2 which permits the use of millimeter-thick matrices [18]. This effect is attributed to the orders-of-magnitude larger crystallite grain sizes achieved in rapid vapor deposition of pH2; the grain sizes are roughly 100 μ m in solid pH₂ versus ~ 100 nm in noble gas matrices [18]. This permits utilization of low guest concentrations that are in the true matrix isolation limit, allowing for the unambiguous identification of monomer spectroscopic features. Further, the increased pathlength allows weaker absorptions such as combination bands and overtones to be measured to provide information beyond the double harmonic approximation. Another advantage to solid pH2 is that infrared transitions of the solid pH2 matrix itself can be used to quantify the thickness of the sample [19], the fraction of hexagonal closest packed crystal sites [20], and the concentration of ortho-hydrogen molecules [21] which make quantitative infrared spectroscopy possible.

We chose to focus on diborane (B2H6) because it has three-center, two-electron banana bonds that provide a stringent test of computational methods. For example, for the bridge B-H stretch/ring deformation mode ν_{17} there is a -155.2 cm⁻¹ shift between the harmonic (ω_{17} = 1758.5 cm $^{-1}$) and anharmonic ($\nu_{17}=1603.3~\text{cm}^{-1}$) frequencies suggesting a scaling factor $\nu_{13}=0.91~\omega_{17}$ which indicates significantly greater anharmonicity for this bonding motif than standard twoelectron, two-center covalent bonds [22]. Furthermore, with two naturally abundant boron isotopes, 0.801 $^{11}\mathrm{B}$ and 0.199 $^{10}\mathrm{B}$, each sample contains the $^{11}B_2H_6$, $^{11}B^{10}BH_6$, and $^{10}B_2H_6$ isotopologues in relative abundances of 0.642(11), 0.319(14), 0.0396(28), respectively, and the IR absorptions of each isotopologue should be resolved in the spectra and thus permit the isotopic shifts to be measured; this is very helpful in testing vibrational assignments. We also chose B₂H₆ because recently the IR spectrum of B₂H₆ (and B₂D₆) trapped in a neon matrix was published permitting detailed comparisons [23]. The final reason we chose B₂H₆ is because we are currently investigating the 193 nm photochemistry of B₂H₆ dispersed in solid pH₂ to synthesize the fluxional BH5 chemical intermediate, and a knowledge of the IR spectrum of the precursor or parent molecule is extremely helpful in making assignments of new features that are produced after photolysis.

The IR spectrum of diborane has been studied extensively both experimentally and by theoretical approaches in the gas-phase. Experimental infrared spectroscopic studies of diborane started with Stitt who measured the gas phase spectrum from 400 to 4000 cm⁻¹ with a prism spectrometer and attempted to analyze the spectrum with an ethane-like structure [24]. Bell and Longuet-Higgins developed a normal coordinate treatment for the bridge model of diborane and assigned fifteen out of seventeen active fundamentals (infrared [24] and Raman [25]) in B₂H₆ with an average error of 2 % and a maximum error of 6 % [26]. Price reexamined the infrared spectrum of diborane with slightly higher resolving power and revealed features that ruled out the ethane-type structure in favor of the bridge model [27,28]. After the bridge structure of diborane was established, the emphasis switched to making an unequivocal assignment of all fundamentals and the determination of high precision ground state molecular constants. In 1970 Lafferty and co-workers [29] used a grating spectrometer (res = $0.04-0.05 \text{ cm}^{-1}$) to measure the rotationally resolved spectrum of ν_8 and ν_{16} , the two infrared active terminal B-H stretching bands, in which samples were enriched in ¹⁰B and ¹¹B which led to the determination of precise ground state rotational constants. Starting in the 1980s Duncan and his collaborators began a series of spectroscopic studies [30-35] of both gaseous and crystalline diborane to establish an assignment of all fundamentals of B₂H₆ and B₂D₆. The goal of these studies was to develop a physically realistic, numerically precise harmonic potential function for diborane [31]. However, given the importance of anharmonic resonances in this molecule, which were not fully appreciated at this time, significant deviations in the predictions of the harmonic potential remained, especially for the bridge B-H stretching modes. As discussed by Stanton [36], since diborane has eight atoms, an exclusively spectroscopic determination of its anharmonic potential is a nearly an intractable problem. Hence, as far back as 1998 it was recognized that only theory can help resolve the question of whether the poor agreement between the predictions of Duncan's empirical potential and the available ab initio calculations for the bridge B-H stretching modes in B2H6 (B₂D₆) is due to limitations in the theoretical description of the dynamics or to surprisingly large anharmonic effects.

Paralleling the developments of increased resolving power in infrared spectroscopy, progress in ab initio methods to calculate the potential energy surface (PES) and methods to calculate the nuclear dynamics on that PES have steadily advanced. In the beginning ab initio methods were employed extensively to compute the vibrational spectrum of B₂H₆, but most calculations were limited to the harmonic approximation, which is of limited utility for this strongly anharmonic molecule. In 1988 Stanton and Gauss [36] used coupled-cluster theory with a reasonably large basis set to obtain cubic and semi-diagonal quartic force constants to calculate the fundamental frequencies of ¹¹B₂H₆. In this work they showed that the differences between ab initio harmonic frequencies for v_6 (b_{2g}) and v_{17} (b_{3u}) and those calculated using the empirical harmonic force field developed by Duncan and co-workers are the result of unexpectedly large anharmonic effects, especially for the ring stretching modes of diborane [36]. In 2012, Begue et al. computed harmonic potential terms at the coupled-cluster level and anharmonic terms at the level of density functional theory, namely B3LYP/6-31 + G*, and used variational and combined variationperturbation approaches to calculate the IR spectrum of B2H6 and B₂D₆ beyond the harmonic limit [37]. In many cases they obtained good agreement between their calculations and their own gas-phase measurements, but for example, they predict the ν_{17} mode at 1567 cm⁻¹ while it is observed at 1604 cm⁻¹, a difference of nearly 40 cm⁻¹ (2.49 %). As recently as 2016 Peng et al. used second-order vibrational perturbation theory (VPT2) based on a quartic force field to calculate the vibrational spectra of B_2H_6 and B_2D_6 in combination with new Ne matrix isolation studies by the same group [23]. The authors report that the mean deviation between the best experimental data for the free

molecule, that is the vibrational frequencies listed in Duncan et al. [31], and the calculated anharmonic frequencies of all the fundamental modes is $+28.8\pm30~\text{cm}^{-1}$ for $^{11}B_2H_6$ and $+13.8\pm18.4~\text{cm}^{-1}$ for $^{11}B_2D_6$. The agreement between calculated and observed wavenumbers is clearly only moderate with discrepancies much larger than the precision of the measurements.

In 2019 Ziegler and Rauhut published a theoretical study on the fundamental modes of ¹¹B₂H₆, ¹¹B₂D₆, ¹⁰B₂H₆, and ¹⁰B₂D₆ in which they calculated the potential using coupled-cluster theory and truncated after 4-mode coupling terms to represent the PES [22]. An optimized modal basis was obtained by vibrational self-consistent field (VSCF) theory and VCI calculations were used to determine vibrational correlation effects and accurate state energies. The mean absolute errors (MAE) between the "best experimental frequencies" (same set as above [31]) and their calculated wavenumbers of the fundamental modes is 4.71 cm⁻¹ for $^{11}\text{B}_2\text{H}_6$ and 6.32 cm $^{-1}$ for $^{11}\text{B}_2\text{D}_6$. The improved agreement between the calculated and observed spectrum compared to Peng et al. [23] is likely due to improved accuracy in the calculated anharmonic frequencies, but they also used 1880 cm⁻¹ for the experimental frequency of v_{13} (b_{1u}) to calculate the MAE of ¹¹B₂H₆ while Duncan lists the deperturbed value, 1924.8 cm⁻¹, in his publication [31]. This highlights the current state of our understanding of the vibrational spectrum of diborane; Duncan's analysis underestimated the anharmonic contributions to the vibrational modes of diborane, especially for the modes involving bridged B-H bonds, and good agreement between theory and experiment waited until theory could accurately represent the anharmonic vibrational dynamics. We therefore decided to perform similar anharmonic vibrational calculations for all three naturally occurring isotopologues of B2H6 and B₂D₆, that is including the ¹¹B¹⁰BH₆ and ¹¹B¹⁰BD₆ non-centrosymmetric isotopologues that were not included in the original publication of Ziegler and Rauhut [22], to compare with new pH2 matrix isolation infrared studies of diborane to determine how well current computational methods can reproduce the vibrational spectrum of diborane and hopefully complete vibrational assignments that started over 70 years ago.

2. Methods

2.1. Experimental details

The experimental apparatus, which combines a high-resolution Fourier Transform Infrared (FTIR) spectrometer with a liquid helium bath cryostat, has been described in detail elsewhere [38,39]. In brief, we grow chemically doped pH₂ crystals on a BaF₂ optical substrate using the rapid vapor deposition (RVD) technique developed by Fajardo and Tam [21,40]. Sample temperatures reported in this study are measured with a Si-diode attached to the bottom of the substrate holder (T_B) ; temperatures are measured at 1 Hz and saved to a computer. In these experiments, unless stated otherwise, 99.97 % pH₂-enriched solids are prepared during deposition by passing normal-H2 gas through a homebuilt ortho/para converter operated near 14 K. The concentration of diborane in the pH2 solid is controlled by varying the guest flow rate with respect to the pH₂ flow rate, which is set to a constant value of 308 (16) mmol/h for this set of experiments. Because of the large range of integrated intensities (e.g., 0.84 to 414.41 km/mol) for the eight infrared active fundamentals of B2H6, six different B2H6/pH2 and five B₂D₆/pH₂ samples with diborane concentrations that range from 1.40 (6) to 123(4) ppm were deposited and analyzed in this study. Experimental details for each of the samples are gathered in Tables S1 and S2 in the Supplementary Information.

High-resolution IR spectra are recorded using an FTIR spectrometer (Bruker IFS-120/5-HR) with the IR beam focused through the cryostat and recollimated with off-axis parabolic mirrors (8" effective focal length) in a transmission optical setup. Two different FTIR setups were employed in this work: (1) IR spectra from 1820 to 6000 ${\rm cm}^{-1}$ at 0.02 ${\rm cm}^{-1}$ resolution were recorded using a tungsten source, KBr beam

splitter, and InSb detector and (2) spectra from 650 to 4700 $\rm cm^{-1}$ at 0.03 $\rm cm^{-1}$ resolution are measured using a glow bar source, KBr beam splitter, and MCT detector. We report spectroscopically determined dopant concentrations in parts per million (ppm) using the following equation,

$$[X] = \frac{(\ln 10)V_0(1 \times 10^6)}{\varepsilon_X d} \int A_{10}(\widetilde{\nu})d\widetilde{\nu}$$
 (1)

where X is the species of interest, $A_{10}(\widetilde{\nu})$ is the decadic absorbance as a function of wavenumber, ε_X is the integrated absorption coefficient for the transition, d is the IR pathlength through the pH₂ crystal determined from the integrated intensity of the Q₁(0) + S₀(0) and S₁(0) + S₀(0) double transitions of solid pH₂ [19], and V_0 is the molar volume of solid pH₂ at liquid helium temperatures (23.16 cm³ mol⁻¹) [41]. The integration limits used in this work are reported in Table S3 and S4 in the Supplementary Information and all B₂H₆ (B₂D₆) concentrations are determined using the ν_8 fundamental.

In this study we investigate both reversible and irreversible changes in the diborane spectral features over the temperature range 1.5 to 4.3 K. As documented in numerous previous studies [42–47], the RVD method is known to produce polycrystalline as-deposited pH₂ solids that contain metastable face-centered cubic (fcc) and hexagonal closest packing (hcp) crystal structures. Warming the sample to greater than 3.5 K for several minutes irreversibly anneals the solid to a nearly pure hcp crystal structure and results in a high degree of alignment of the c-axis of the hcp crystallites with the substrate surface normal [43,44]. This annealing process can be quantified [46–48] by measuring the fraction of hcp crystal structures in the probe region, $X_{hcp} = N_{hcp}/(N_{hcp} + N_{fcc})$, using the zero phonon $U_0(0)$ solid pH₂ single transition near 1167.1 cm $^{-1}$ or the $U_1(0)$ transition near 5261.29 cm $^{-1}$. Only pH₂ molecules in hcp crystal sites that lack a center-of-inversion can contribute to the integrated intensity of the $U_0(0)$ or $U_1(0)$ transitions such that the integrated intensity can be used to monitor X_{hcp} using the following

$$X_{hcp} = 2.303 \frac{cV_0}{\widetilde{\alpha} d\widetilde{\nu}_0 N_A} \int A_{10}(\widetilde{\nu}) d\widetilde{\nu}$$
 (2)

where c is the speed of light *in vacuo*, $\tilde{\alpha}$ is the $U_0(0)$ or $U_1(0)$ absorption coefficient, d is the thickness of the sample or the pathlength, N_A is Avogadro's constant, and $\tilde{\nu}_0$ is the peak frequency of the transition in cm⁻¹. Consequently, X_{hcp} should have values between 0 and 1 and can be used to quantify the crystallinity of the sample.

2.2. Computational details

Frozen core explicitly correlated coupled-cluster theory [49], i.e., CCSD(T)-F12a, in combination with a triple- ζ basis set [50], cc-pVTZ-F12, has been used to determine the equilibrium structure, harmonic frequencies and large parts of the multidimensional PES. An n-mode expansion of the PES employing rectilinear normal coordinates and being truncated after the 4-mode coupling terms has been used in all calculations. A multi-level scheme [51] has been utilized to reduce the computational effort, that is, the 3D and 4D terms were evaluated by using an orbital basis set of double- ζ quality, i.e., cc-pVDZ-F12. Symmetry has been exploited two-fold, first in the electronic structure calculations and secondly in the construction of the PES [52]. Dipole moment surfaces (DMS) were evaluated using the distinguishable cluster approximation [53], DCSD, with the same basis sets. The grid representation of the PESs and DMSs were transformed to an analytical representation using 7 monomials per mode. Kronecker product fitting has been used for this task [54].

Vibrational one-mode wavefunctions (modals) were obtained from vibrational self-consistent field theory (VSCF) and serve as basis functions in the subsequent correlation calculations. Vibrational configuration interaction theory [55–57] including up to sextuple-excitations and

a further restriction of the correlation space by including only those Hartree products with a maximal excitation per mode up to 7th root and a maximal sum of vibrational quantum numbers of 15. This resulted in about 13 million configurations per irreducible representation and vibrational state calculation. The μ -tensor, as occurring in the Watson Hamiltonian [58], was truncated after 0th-order to account for vibrational angular momentum contributions. All calculations have been performed with the Molpro package of ab initio programs [59].

3. Results

Diborane, B2H6 (B2D6), is the simplest stable borohydride under ambient conditions [60]. Diborane has a ring-type molecular structure and has two bridging hydrogens and four terminal hydrogens. B2H6 and B_2D_6 have D_{2h} point group symmetry and eighteen vibrational modes [61] that transform as $4a_g$, $2b_{1g}$, $2b_{2g}$, $1b_{3g}$, $1a_u$, $2b_{1u}$, $3b_{2u}$, and $3b_{3u}$. Eight of the modes are infrared active $(2b_{1u}, 3b_{2u}, \text{ and } 3b_{3u})$ and nine of the modes are Raman active $(4a_g, 2b_{1g}, 2b_{2g}, 1b_{3g})$, with one mode $(1a_u)$ that is neither infrared nor Raman active. The ¹⁰B¹¹BH₆ (¹⁰B¹¹BD₆) isotopologues belong to the $C_{2\nu}$ point group that is not centrosymmetric, such that sixteen of the total eighteen vibrational modes are formally infrared active [23]. However, none of the new infrared active modes in the mixed boron isotopologues absorb strongly. We do observe peaks that are assigned to several of these new active vibrational modes (ν_3 , ν_1 , and ν_{11} for $^{10}B^{11}BH_6$ and ν_{15} , ν_1 , and ν_{11} for $^{10}B^{11}BD_6$) for the mixed boron isotopologues that are symmetry forbidden in the case of ¹¹B₂H₆ or ${}^{10}B_2H_6$, but in general the infrared intensities of ${}^{10}B^{11}BH_6$ (${}^{10}B^{11}BD_6$) follow closely with the higher symmetry isotopologues.

In this work we use the generally accepted numbering of the diborane normal mode vibrations for the molecular point group D_{2h} that conforms to the notation for ethylene which was originally used by Bell and Longuet-Higgins to predict the bridged structure of diborane [26]. This is also the vibrational mode numbering scheme adopted by Duncan in his extensive spectroscopic studies of diborane and its isotopologues [30–35]. In this axis system, I^l , the b_{1u} vibrations are c-type, the b_{2u} vibrations are b-type, and the b_{3u} modes are a-type. More recent spectroscopic work [23] and the NIST webbook [62] utilize the more

conventional mode numbering scheme which effects the symmetry species by interchanging the 1 and 2 subscripts in the symmetry symbols and/or requires renumbering of nine ($\nu_6 - \nu_{14}$) of the eighteen fundamentals to conform to this competing convention. To avoid possible confusion, we include Tables S5 and S6 in the Supplementary Information to show how the different vibrational mode numbering schemes are related.

3.1. B₂H₆ and B₂D₆ fundamental vibrations

Fig. 1 shows survey spectra from 700 to 3000 cm⁻¹ where five of the eight IR active fundamentals of both B2H6 and B2D6 are observed. The pH₂ matrix isolation spectra are dominated by the intense fundamental at 1597 cm⁻¹ (1194 cm⁻¹) for B_2H_6 (B_2D_6) which corresponds to ν_{17} (bridge BH stretch/ring deformation) where it has been suggested that the large intensity of this band is associated with the tendency toward the formation of BH₂BH₄ and BH₄BH₂ at the turning points of this vibration [28]. The end-over-end rotation of diborane is quenched when it is trapped in the pH₂ matrix and thus there is no rotational fine structure associated with these spectra (more on this later). Shown at the bottom of each spectrum are the calculated ¹¹B₂H₆ (¹¹B₂D₆) vibrational frequencies from the VCI calculations which show quantitative agreement with the experimentally observed peak frequencies and permit straightforward assignment of the fundamental vibrational modes. Table 1 lists the wavenumbers of the absorption lines in the infrared spectrum of B₂H₆ isolated in an as-deposited pH₂ matrix at 1.8 K along with Ne matrix isolation results [23] recorded at 4 K to permit comparisons; Table 2 presents the analogous comparisons for B₂D₆/pH₂. At these B_2H_6 (B_2D_6) concentrations where the ν_{17} decadic absorption is kept below 1.0; the spectrum is quite sparse due to the centrosymmetric molecular structure of diborane which results in vibrations being either IR or Raman active; ten of the eighteen normal modes of the ¹¹B₂H₆ and ¹⁰B₂H₆ species are IR inactive. At higher B₂H₆ (B₂D₆) concentrations we observed one more fundamental (ν_{13} – bridged BH stretch/ring deformation) and several combination bands for both species.

We now present the spectroscopic assignments of B_2H_6 trapped in solid pH_2 in more detail by showing spectra in expanded regions

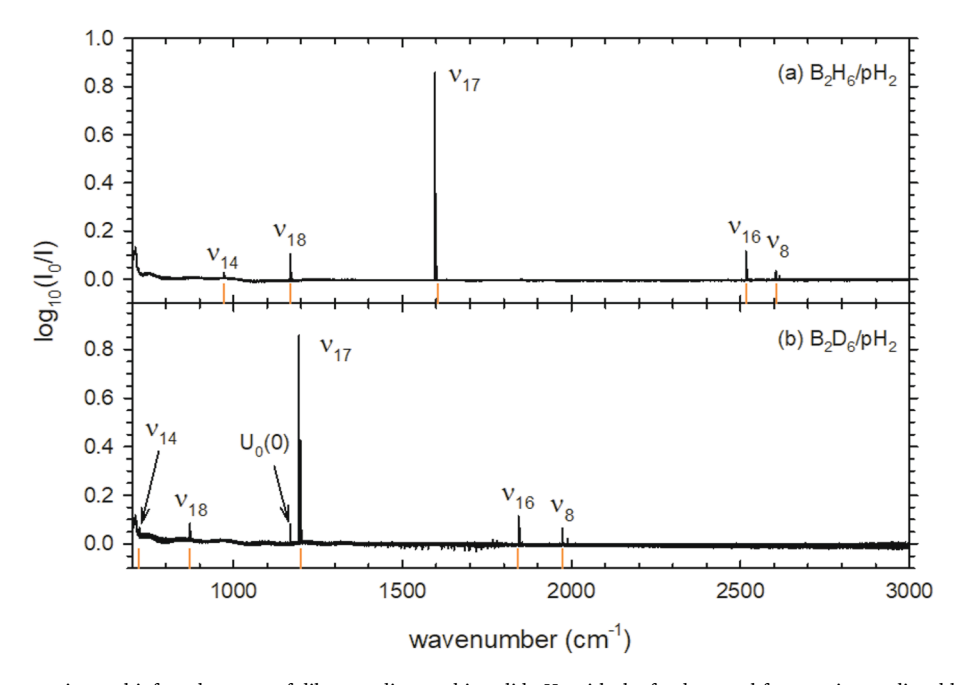


Fig. 1. Comparison of the experimental infrared spectra of diborane dispersed in solid pH_2 with the fundamental frequencies predicted by anharmonic vibrational calculations. Spectra recorded at 1.8 K for as-deposited samples (a) of B_2H_6/pH_2 with d=0.174(2) cm and $[B_2H_6]=1.40(6)$ ppm, and (b) B_2D_6/pH_2 with d=0.125 (1) cm and $[B_2D_6]=3.6(3)$ ppm. The gold lines at the bottom of each spectrum are the calculated peak positions for $^{11}B_2H_6$ and $^{11}B_2D_6$, respectively, for the labeled mode.

Table 1 Infrared absorptions of B_2H_6 in as-deposited pH_2 solids at 1.8 K compared to B_2H_6 1:1000 in Ne at 4 K. Peak positions in cm⁻¹.

			pH_2				Ne	
mode	Sym.	¹¹ B ₂ H ₆	$^{11}B^{10}BH_{6}$	$^{10}B_2H_6$	mode ^a	$^{11}B_2H_6$	$^{11}B^{10}BH_{6}$	¹⁰ B ₂ H ₆
ν ₉	b_{2u}				ν_{13}	920.10	923.98	
ν_{14}	b_{1u}	972.12	974.67	976.84	ν_9	974.75	977.25	979.37
ν_{18}	b_{3u}	1169.16	1171.74	1175.61	ν_{18}	1172.10	1174.71	1178.56
ν_3	b_{1u}		1184.38		ν_3			
ν_{17}	b_{3u}	1596.80	1599.02	1601.14	ν_{17}	1597.73	1599.96	1602.09
ν_{13}	b_{1u}	1878.42	1881.83	1885.37	ν_8	1877.87	1882.41	1884.93
ν 16	b_{3u}	2516.98	2519.01	2522.30	ν_{16}	2521.77	2523.84	2526.38
ν_1	a_{g}		2532.36		ν_1			
ν_{11}	b_{1g}		2597.03		ν_6			
ν_8	b_{2u}	2604.93	2615.06	2618.68	ν_{12}	2610.62	2620.67	2624.49
$\nu_9 + \nu_{15}$	b_{1u}	1989.99	1993.78	1997.41	$\nu_{13} + \nu_{15}$	1990.24	1993.65	1996.16
$2\nu_{18}$	a_{g}		2336.68		$2\nu_{18}$			
$\nu_3 + \nu_{18}$	b_{3u}	2339.35	2347.22	2350.54	$\nu_3 + \nu_{18}$	2344.90	2352.98	2356.17
$\nu_4 + \nu_{17}$	b_{3u}	2372.99	2389.55	2405.99	$\nu_4 + \nu_{17}$	2373.12	2389.28	
$\nu_5 + \nu_6$	b_{2u}	2628.49	2631.73	2634.77	$\nu_5 + \nu_{10}$			
$\nu_7 + \nu_{17}$	b_{1u}	2463.61	2473.01	2482.74	$\nu_{11} + \nu_{17}$			
$\nu_3+\nu_{17}$	b_{1u}	2777.44	2783.09	2787.74	$\nu_3+\nu_{17}$			

^a vibrational mode assignments from Ref. [23].

Table 2 Infrared absorptions of B_2D_6 in as-deposited p-H₂ solids at 1.8 K compared to B_2D_6 1:1000 in Ne at 4 K. Peak positions in cm⁻¹.

			pH_2				Ne	
mode	Sym.	$^{11}B_2D_6$	$^{11}B^{10}BD_{6}$	$^{10}B_2D_6$	mode ^a	$^{11}B_2D_6$	$^{11}B^{10}BD_{6}$	$^{10}B_2D_6$
ν ₉	b_{2u}				ν_{13}			
ν_7	b_{3g}		719.31		ν_{11}		720.65	
ν_{14}	b_{1u}	722.03	728.46	725.84	ν_9	723.15	723.52	724.76
ν_{18}	b_{3u}	871.78	874.23	877.72	ν_{18}	873.79	876.25	879.75
ν_{17}	b_{3u}	1194.42	1197.85	1201.05	ν_{17}	1195.00	1198.44	1201.65
ν_{13}	b_{1u}	1476.54	1482.63	1488.19	ν_8	1475.25	1481.41	1486.90
ν_{16}	b_{3u}	1843.35	1847.71	1854.76	ν_{16}	1846.52	1850.74	1857.96
ν_1	a_{g}		1874.36		ν_1	1848.97	1852.73	1860.37
ν_{11}	b_{1g}		1965.69		ν_9		1968.84	
ν_8	b_{2u}	1973.54	1987.67	1994.15	ν_{12}	1977.20	1990.91	1997.66
$\nu_5 + \nu_{15}$	b_{3u}	1318.10	1318.10	1318.10	$\nu_5 + \nu_{15}$	1321.32	1323.08	
$\nu_9 + \nu_{15}$	b_{1u}	1396.43	1399.78	1403.30	$\nu_{13} + \nu_{15}$	1396.94	1400.40	1404.02
$\nu_3 + \nu_{18}$	b_{3u}	1768.09	1779.77	1789.91	$\nu_{3} + \nu_{18}$	1770.91	1782.51	1792.50
$2\nu_3$	a_{g}		1822.59		$2\nu_3$			
$\nu_{12} + \nu_{17}$	b_{2u}°	1927.29	1937.06	1944.14	$\nu_4 + \nu_{17}$			

^a vibrational mode assignments from Ref. [23].

centered around the fundamental absorptions of B2H6 in Fig. 2. For example, the v_{14} fundamental (b_{1u} , terminal BH in-phase wag) of B_2H_6 is a c-type band that is observed near 972 cm⁻¹ for B₂H₆ solvated in solid pH₂. The three observed features in this region correspond to the ${}^{11}B_2H_6$, $^{10}B^{11}BH_6$, and $^{10}B_2H_6$ isotopologues in natural abundance (e.g., 16.2:8.06:1). These three isotopologue peaks are labeled by the frequency comb near the top of Fig. 2 with i, ii, and iii designating the $^{11}\text{B}_2\text{H}_6$, $^{10}\text{B}^{11}\text{BH}_6$, and $^{10}\text{B}_2\text{H}_6$ isotopologue peaks, respectively. The ν_{14} fundamental of B₂H₆ in Fig. 2 shows the "normal" boron isotopic shift pattern; a normal boron isotopic shift pattern is one where the ¹¹B₂H₆ peak wavenumbers are lower than ${}^{10}B_2H_6$, and the ${}^{10}B^{11}BH_6$ peak lies midway between the ¹¹B₂H₆ and ¹⁰B₂H₆ peaks. Also shown in Fig. 2 is the calculated v_{14} spectrum which is represented by three Lorentzian lineshapes that were constructed using the output of the VCI calculations (wavenumbers and intensities) and a full width half maximum (FWHM) chosen to match the experimental spectrum. The calculated VCI frequencies and intensities for all three boron isotopologues of both B2H6 and B2D6 are given in Table 3 and 4, respectively. The agreement between the experimental and calculated spectra is quite good for the six IR-active B₂H₆ fundamentals in Fig. 2; the greatest discrepancy is for the v_{17} mode which involves the bridging B-H-B bonds and is expected to be very anharmonic (more on this later). We will quantify the comparison between theory and experiment in the discussion section, and for now we will use the predicted spectrum to help guide the assignment of the observed B2H6 features.

Examination of Fig. 2 shows that for the most part, we observe repeated three peak isotopic splitting patterns for all six of the B_2H_6 fundamentals, which suggests that if B_2H_6 occupies multiple matrix sites in solid pH2, the site splitting's are smaller than the boron isotopic shifts for the three B_2H_6 isotopologues. Both ν_8 and ν_{13} have noticeably broader lineshapes (FWHM $\approx 0.65~\text{cm}^{-1}$) than the other fundamentals; $\nu_{14}, \nu_{18}, \nu_{17},$ and ν_{16} all have narrower linewidths (FWHM $\leq 0.25~\text{cm}^{-1}$) and show evidence for additional matrix site splitting's (for example, see ν_{16} in Fig. 2). To help identify perturbations and mixing caused by anharmonic resonances, we present the percentages of the contributing configurations (Hartree products) to the eighteen fundamentals and several two-quanta combination bands and overtones in Tables S7 and S8 for boron isotopologues of B_2H_6 and B_2D_6 , respectively, in the Supplementary Information.

We applied this same type of assignment procedure to the infrared spectra of B_2D_6 trapped in solid pH_2 . Once again, we rely on the VCI calculations to guide the assignment and to help identify perturbations. We show expanded views of the six observed B_2D_6 fundamental modes in Fig. 3. Assignment of all six fundamentals is readily accomplished via comparison to theory. Like B_2H_6 , the VCI calculations reproduce the B_2D_6/pH_2 experimental spectra very well for the IR-active vibrational fundamentals. However, with B_2D_6 we see the first indication of perturbations in the vibrational spectrum. The ν_{14} spectrum of B_2D_6 shows

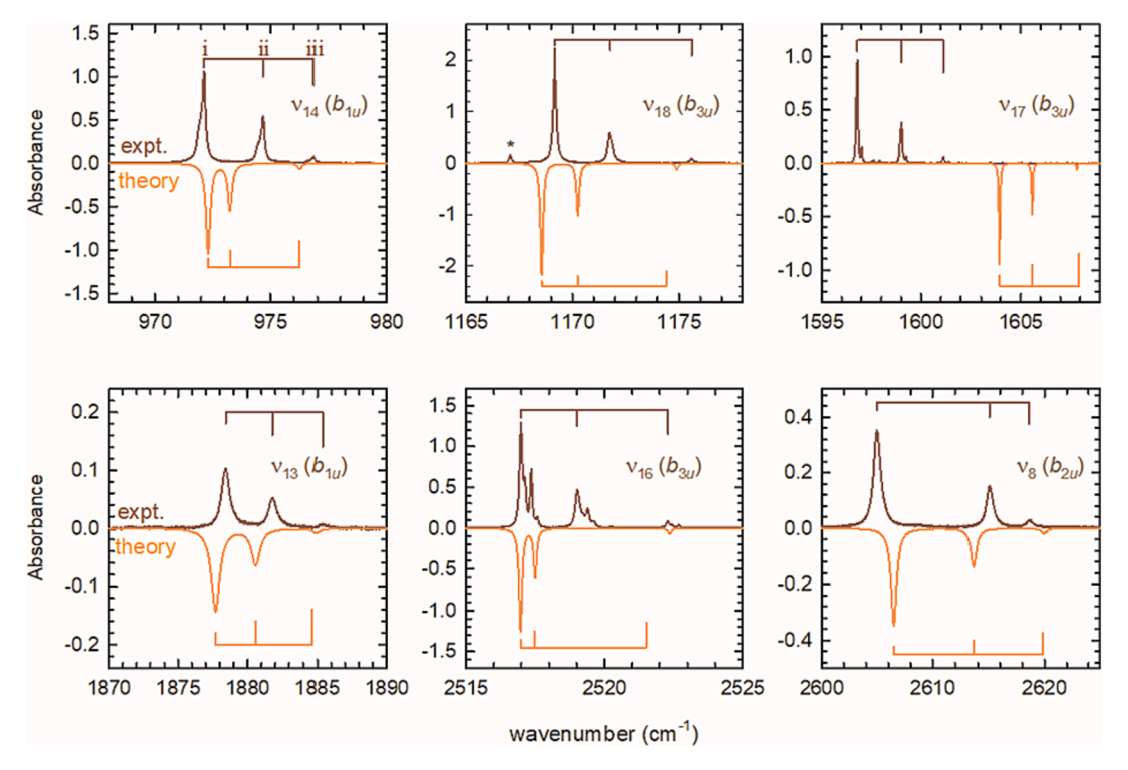


Fig. 2. Comparison of the six B_2H_6/pH_2 fundamental absorptions observed (expt.) in this study with the corresponding calculated (theory) spectra. The tick lines indicate the specific boron isotopologue assignment with i, ii, and iii designating $^{11}B_2H_6$, $^{10}B^{11}B_1H_6$, and $^{10}B_2H_6$, respectively, where the labels shown in the n_{14} spectrum apply to all as indicated by the varying length of the tick lines. Spectra are simulated using the experimental B_2H_6 concentration and sample thickness, and a Lorentzian lineshape with the FWHM determined from the observed spectra. The asterisk in the ν_{18} spectrum designates the $U_0(0)$ pure rotational ($J=4\leftarrow0$) transition of solid pH_2 and is not a B_2H_6 absorption.

anomalous boron isotopic shifts and the VCI calculations reproduce this anomaly (see Fig. 3). Specifically, the ν_{14} peak frequency for $^{10}\text{B}_2\text{D}_6$ is at lower wavenumbers than ¹⁰B¹¹BD₆. This is due to a weak anharmonic coupling between the ν_{14} (b_2) and ν_7 (b_2) modes of the unsymmetrical species ¹⁰B¹¹BD₆ that is symmetry forbidden for the symmetric species 11 B₂D₆ and 10 B₂D₆, i.e., ν_{14} (b_{1u}) and ν_{7} (b_{2g}). In support for this finding, we observe the IR-inactive ν_7 fundamental of $^{10}B^{11}BD_6$ at 719.31 cm $^{-1}$ because this mode steals intensity from the nearby v_{14} mode (see the v_7 peak in Fig. 3). This mixing pushes the ν_{14} state higher in energy and the ν_7 state lower in energy just for the $^{11}B^{10}BD_6$ isotopologue, and this is the cause of the anomalous boron isotopic splitting pattern for the ν_{14} fundamental. Thus, anharmonic perturbations in the vibrational spectrum of B_2D_6 can be comparable in magnitude to the boron isotopic shifts in the various fundamental vibrations, and in several cases anharmonic coupling present in the ¹⁰B¹¹BD₆ isotopologue that is absent in the centrosymmetric isotopologues results in these anomalies. At a finer level of detail there are matrix site splitting's apparaent in some of the fundamental spectra of B2H6 and B2D6, and we examine site splitting's in more detail in the next section.

3.2. Annealing B_2H_6/pH_2 samples

One of the advantages that solid pH₂ offers over noble gas matrices is that the large amount zero-point energy present in the quantum crystal makes it easier to anneal and prepare homogeneous crystal structures with large grain sizes. Like noble gas crystals, rapid vapor deposited solid pH₂ contains both fcc and hcp crystal domains that differ by small amounts of energy, such that both crystal structures are typically present in chemically doped as-deposited pH₂ samples. However, raising the temperature to \sim 3.5 K after deposition rapidly converts (\sim 30 min) the higher energy fcc crystal structure to the lower energy hcp form which can be quantified by monitoring the $U_0(0)$ or $U_1(0)$ transitions of solid pH₂ as discussed in Section 2. Thus, the first time the temperature of a

RVD sample is raised above ~ 3.5 K the sample starts to irreversibly convert the mixed fcc/hcp crystal structure to pure hcp. This annealing process also likely removes crystal defects but much less is known about defects in solid pH $_2$ because of the lack of applicable structural techniques. Once the sample has been annealed, temperature cycling the sample can be used to look for reversible changes in the spectra with temperature. These changes in the spectra of annealed samples usually consist of shifts in the populations of different matrix sites.

We illustrate these types of population changes after annealing using the ν_{16} and ν_{8} spectra of B₂H₆ in solid pH₂ shown in Fig. 4. Trace (a) in Fig. 4 shows the ν_{16} and ν_{8} spectra for an as-deposited pH₂ sample that were used to determine the vibrational frequencies of the different B₂H₆ isotopologues. We see that ν_{16} shows fine structure while the ν_{8} peaks do not. We interpret this as follows: the v_{16} lineshape is much narrower than v_8 and thus it is easier to detect matrix site splitting's using this mode. As seen in Fig. 4, the effects of annealing on the v_{16} absorption features are shown by comparing trace (a) with (c), where it is observed that the intensity of each isotopologue shifts from a lower frequency peak to a higher frequency peak. In the as-deposited sample the dominant ${}^{11}B_2H_6$ ν_{16} peak is observed at 2516.98 cm $^{-1}$ while in the low temperature annealed sample, the most prominent peak is at 2517.59 cm⁻¹. This indicates that the matrix site splitting's are on the order of $0.61 \,\mathrm{cm}^{-1}$ for v_{16} and that the population of different matrix sites change considerably upon annealing the as-deposited crystal.

There are both reversible and irreversible changes in the B_2H_6/pH_2 spectra with temperature cycling after annealing. As shown in Fig. 4, after the sample is annealed, temperature cycling between low and high temperatures produces reversible changes in the ν_{16} and ν_{8} spectra. There also is some irreversible growth in small absorptions to the red of the major ν_{16} features, but otherwise the changes are fully reversible. After the sample is annealed, the intensity shifts between four $\nu_{16}^{11}B_2H_6$ features as follows; at high temperatures two peaks at lower wavenumbers (2516.98 cm⁻¹ and 2517.37 cm⁻¹) grow in intensity and the

 $\label{eq:table 3} VCI\ calculated\ anharmonic\ vibrational\ wavenumbers\ (cm^{-1})\ and\ intensities\ (km/mol)\ for\ the\ three\ ^{11/10}B\ isotopologues\ of\ B_2H_6.$

mode	(sym.)	description	$^{11}B_{2}H_{6}$	$^{10}B^{11}BH_{6}$	$^{10}B_{2}H_{6}$
ν_1	(a_g)	t-BH $_2\ sym.\ str.$	2528.07	2528.60	2534.57
			(0.00)	(7.22)	(0.00)
ν_2	(a_g)	b-BH ring	2112.19	2109.22	2110.31
		breathing	(0.00)	(0.00)	(0.00)
ν_3	(a_g)	t-BH ₂ scis.	1179.36	1182.59	1185.01
	(~)	D. D. otmotoh	(0.00)	(4.09)	(0.00)
ν_4	(a_g)	B-B stretch	787.43	801.34	815.64
•	(a.)	t-BH ₂ twist	(0.00)	(0.03) 828.40	(0.00)
ν_5	(a_u)	t-bri ₂ twist	828.81 (0.00)	(0.00)	828.39 (0.00)
ν_6	(b_{2g})	b-BH ring	1791.71	1793.43	1796.51
7 0	(02g)	stretch	(0.00)	(0.00)	(0.00)
ν_7	(b_{2g})	t-BH ₂ wag	868.71	865.10	876.51
.,	287	2 0	(0.00)	(0.03)	(0.00)
ν_8	(b_{2u})	t-BH2 anti-sym.	2606.49	2613.64	2619.86
		str.	(159.88)	(129.28)	(149.49)
ν_9	(b_{2u})	t-BH ₂ in-phase	938.69	941.05	942.73
		rock	(0.84)	(0.79)	(0.82)
ν_{10}	(b_{2u})	ring pucker	369.35	367.51	367.77
			(14.82)	(14.78)	(14.79)
ν_{11}	(b_{1g})	t -BH $_2$ anti-sym.	2593.89	2594.57	2607.95
		str.	(0.00)	(26.68)	(0.00)
ν_{12}	(b_{1g})	t-BH ₂ out-of-	918.70	919.82	931.27
		phase wag	(0.00)	(0.05)	(0.00)
ν_{13}	(b_{1u})	b-BH ring str.	1877.70	1880.59	1884.66
	<i>a</i> >	. Drr 1 1	(9.61)	(9.70)	(9.89)
ν_{14}	(b_{1u})	t-BH ₂ in-phase	972.30	973.24	976.23
	(h.)	wag	(21.38)	(21.09)	(21.37)
ν_{15}	(b_{3g})	torsion (t-BH ₂ / b-BH ₂)	1017.43	1017.08 (0.00)	1016.95 (0.00)
1/	(b_{3u})	t-BH ₂ sym. str.	(0.00) 2516.97	2517.50	2521.51
ν_{16}	(ν_{3u})	t-D112 synt. str.	(124.41)	(119.63)	(128.71)
ν_{17}	(b_{3u})	b-BH ₂ ring	1603.94	1605.59	1607.95
-1/	(0311)	deform.	(414.41)	(417.28)	(421.58)
ν_{18}	(b_{3u})	t-BH anti-sym.	1168.56	1170.25	1174.41
10	- 04-	deform.	(78.01)	(71.81)	(75.41)
$\nu_{10} + \nu_{12}$	(b_{3u})	Comb. band	1278.34	1280.24	1289.90
			(1.77)	(1.75)	(1.66)
$\nu_{10}{+}\nu_{15}$	(b_{1u})	Comb. band	1375.07	1373.50	1373.79
			(1.40)	(1.41)	(1.44)
$\nu_5+\nu_7$	(b_{3u})	Comb. band	1690.95	1688.12	1699.09
			(0.43)	(0.45)	(0.47)
$\nu_7 + \nu_{14}$	(b_{3u})	Comb. band	1833.28	1831.73	1861.59
	<i>a</i> ,		(3.00)	(3.60)	(15.78)
$\nu_5 + \nu_{15}$	(b_{3u})	Comb. band	1856.38	1855.28	1839.87
** **	(b_{3u})	Comb. band	(13.21)	(12.82)	(0.25)
$\nu_9 + \nu_{12}$	(ν_{3u})	Collid. Dalid	1858.79 (0.00)	1861.75 (0.52)	1876.21 (1.39)
$\nu_9 + \nu_{15}$	(b_{1u})	Comb. Band	1994.56	1997.09	2000.97
P9 P15	(0111)	(FR ν_{13})	(2.51)	(2.70)	(2.96)
$\nu_3 + \nu_{14}$	(b_{1u})	Comb. band	2152.16	2156.45	2161.68
-31-14	(Iu)		(0.09)	(0.08)	(0.09)
$2\nu_{18}$	(a_g)	Overtone	2330.27	2334.04	2342.50
	. 0-		(0.00)	(1.90)	(0.00)
$\nu_3 + \nu_{18}$	(b_{3u})	Comb. band	2336.34	2344.13	2347.06
			(7.39)	(5.69)	(8.72)
$\nu_4+\nu_{17}$	(b_{1u})	Comb. band	2378.99	2394.94	2411.87
			(1.43)	(1.72)	(2.14)
$\nu_5 + \nu_6$	(b_{2u})	Comb. band	2629.04	2630.81	2634.64
			(10.30)	(15.93)	(27.83)
$\nu_7+\nu_{13}$	(b_{3u})	Comb. band	2735.84	2735.96	2750.83
	_		(1.95)	(2.08)	(1.94)
$\nu_6+\nu_{14}$	(b_{3u})	Comb. band	2761.61	2764.57	2770.51
			(0.59)	(0.57)	(0.60)
$\nu_3 + \nu_{17}$	(b_{3u})	Comb. band	2784.37	2789.21	2794.03
- 1 · ·	(h.)	Comb 11	(1.51)	(0.72)	(1.75)
$\nu_1+\nu_{10}$	(b_{2u})	Comb. band		2896.72	
				(0.18)	

Table 4 VCI calculated anharmonic vibration wavenumbers (cm $^{-1}$) and intensities (km/mol) for the three $^{11/10}$ B isotopologues of B_2D_6 .

		D isotopologi	2 0		
mode	(sym.)	description	$^{11}B_{2}D_{6}$	$^{10}B^{11}BD_{6}$	$^{10}B_{2}D_{6}$
ν_1	(a_g)	t-BD sym. str.	1863.51	1873.56	1882.91
•	. 6'	,	(0.00)	(3.90)	(0.00)
ν_2	(a_g)	b-BD ring	1514.86	1515.57	1516.12
- 2	87	breathing	(0.00)	(0.01)	(0.00)
ν_3	(a_g)	t-BD sym.	908.60	918.73	928.08
V 3	(ug)	deformation	(0.00)	(0.14)	(0.00)
ν_4	(a_g)	B-B stretch	708.11	714.95	721.43
V 4	(ug)	D-D stretch	(0.00)	(0.05)	
	(~)	tomoiom (t DD)			(0.00)
ν_5	(a_u)	torsion (t-BD ₂)	591.03	591.03	590.89
			(0.00)	(0.00)	(0.00)
ν_6	(b_{2g})	b-BD anti-sym.	1271.33	1273.42	1275.29
		stretch	(0.00)	(0.00)	(0.00)
ν_7	(b_{2g})	t-BD out-of-	713.50	718.24	729.85
		phase rock	(0.00)	(4.34)	(0.00)
ν_8	(b_{2u})	t-BD anti-sym.	1974.43	1987.67	1995.18
		stretch	(91.37)	(69.84)	(92.88)
ν ₉	(b_{2u})	t-BD in-phase	698.40	700.33	702.96
		rock	(0.32)	(0.31)	(0.30)
/10	(b_{2u})	ring pucker	260.43	260.28	260.33
-			(7.51)	(7.50)	(7.50)
ν_{11}	(b_{1g})	t-BD anti-sym.	1961.33	1965.77	1979.74
	- 187	stretch	(0.00)	(17.65)	(0.00)
Via	(b_{1g})	t-BD out-of-	737.63	743.58	750.69
V ₁₂	(D _{1g})	phase wag			
lia a	(h.)	b-BD ring str.	(0.00)	(0.00)	(0.00)
V ₁₃	(b_{1u})	יוופ אווו מפ-ט וווון אווי	1474.88	1480.81	1486.15
	(h.)	4 DD in -1	(4.94)	(5.14)	(5.85)
V ₁₄	(b_{1u})	t-BD in-phase	721.12	726.48	725.84
		wag	(11.46)	(7.41)	(11.46)
ν_{15}	(b_{3g})	torsion (t-BD /	726.38	726.43	726.25
		b-BD)	(0.00)	(0.00)	(0.00)
ν_{16}	(b_{3u})	t-BD symmetric	1842.29	1846.76	1853.79
		stretch	(82.40)	(75.34)	(75.75)
V17	(b_{3u})	b-BD ring str.	1198.75	1202.22	1205.43
		-	(246.64)	(248.69)	(251.05)
ν_{18}	(b_{3u})	t-BD anti-sym.	871.30	873.70	877.25
10	(- 54)	deform.	(26.50)	(25.17)	(24.30)
$\nu_{10} + \nu_{15}$	(b_{1u})	Comb. band	982.89	983.01	982.98
-10 -15	(O1u)	compr band	(0.60)	(0.61)	(0.62)
tian I tian	(b_{3u})	Comb. band	993.42	999.72	1006.34
$\nu_{10} + \nu_{12}$	(ν_{3u})	Comb. Dand			
	<i>a</i> .)	0	(0.37)	(0.36)	(0.35)
$\nu_5 + \nu_7$	(b_{2u})	Comb. band	1302.37	1307.40	1318.60
	<i>a</i> :	0 1 1 1	(0.21)	(0.13)	(0.21)
$\nu_5 + \nu_{15}$	(b_{3u})	Comb. band	1319.91	1320.12	1319.82
			(4.26)	(4.69)	(4.97)
$\nu_9 + \nu_{15}$	(b_{1u})	Comb. band	1398.44	1402.22	1405.96
		(FR ν_{13})	(4.39)	(4.23)	(4.11)
$\nu_7 + \nu_{14}$	(b_{3u})	Comb. band	1434.09	1441.59	1454.68
			(6.21)	(0.07)	(7.78)
$\nu_9 + \nu_{12}$	(b_{3u})	Comb. band	1437.58	1445.32	1454.86
. 12	. 50		(0.63)	(2.43)	(5.65)
$\nu_3 + \nu_{18}$	(b_{3u})	Comb. band	1766.56	1778.12	1788.25
-318	Cow	(FR ν_{16})	(18.32)	(22.47)	(27.41)
$2\nu_3$	(a_1)	Overtone (FR	1805.09	1820.90	1834.73
 √3	(u ₁)				
u 1 **	(h.)	ν ₁) Comb bond	(0.00)	(0.78)	(0.00)
$\nu_{12} + \nu_{17}$	(b_{2u})	Comb. band	1931.29	1940.25	1950.27
			(4.73)	(5.33)	(5.50)
$\nu_3 + \nu_{17}$	(b_{3u})	Comb. band	2103.21	2116.20	2128.62
			(0.73)	(0.58)	(1.02)
$\nu_4 + \nu_{13}$	(b_{3u})	Comb. band	2180.32	2193.42	2205.16
			(0.16)	(0.15)	(0.17)
$\nu_2 + \nu_{17}$	(b_{3u})	Comb. band	2696.86	2699.87	2705.06
			(6.93)	(6.90)	(7.72)
	<i>a</i> >	Comb. band	2729.42	2739.93	2747.55
$\nu_1 + \nu_{18}$	(b_{3u})				

high frequency peaks (2517.13 cm $^{-1}$ and 2517.59 cm $^{-1}$) decrease in intensity and almost disappear (see Fig. 4 (b) or (d)). At low temperature, the doublet at lower wavenumbers decreases in intensity and the higher wavenumber pair increase in intensity. These intensity changes are best observed using the $^{11}B_2H_6$ ν_{16} peaks but are also evident for the $^{11}B^{10}BH_6$ isotopologue peaks. To better visualize the intensity changes produced with temperature cycling, we show a blow-up view of just the

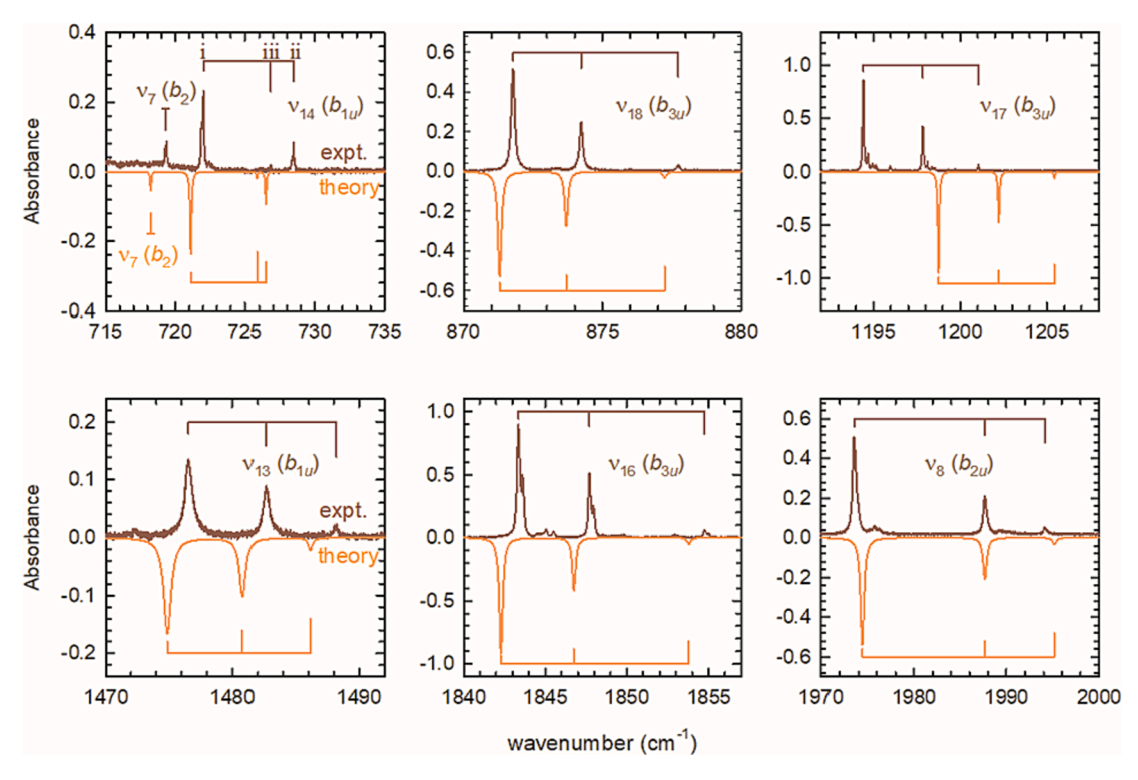


Fig. 3. Comparison of the six B_2D_6/pH_2 fundamental absorptions observed (expt.) in this study with the corresponding calculated (theory) spectra. As in Fig. 2, the tick lines indicate the boron isotopologue assignment. Spectra are simulated using the experimental B_2D_6 concentration and sample thickness, and a Lorentzian lineshape with the FWHM determined from the observed spectra. Note that the spectrum of ν_{14} shows evidence of perturbations, the $^{10}B_2D_6$ peak is at lower wavenumbers than the $^{11}B^{10}BD_6$ peak. See text for further details.

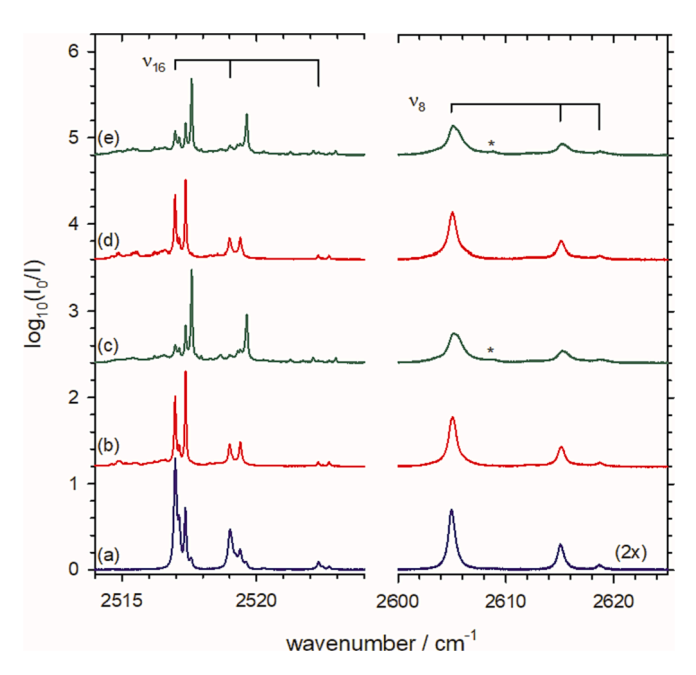


Fig. 4. Infrared spectra of a B_2H_6/pH_2 sample in the region of ν_{16} and ν_8 showing the effects of annealing and temperature cycling. (a) As-deposited sample, recorded at 1.54(1) K, (b) annealed sample, recorded at 3.97(1) K, (c) annealed sample, recorded at 1.56(1) K, (d) annealed sample recorded at 4.00(1) K, and (e) annealed sample recorded at 1.54(1) K. The frequency combs at the top show the boron isotopologue assignments for an as-deposited sample analogous to Fig. 2. The spectra have been offset and the ν_8 spectral intensity has been increased (2x) to make comparisons. Note the growth of the peak at 2608.8 cm⁻¹ marked with an asterisk in the ν_8 spectra recorded at low temperature for annealed samples.

 v_{16} features for $^{11}B_2H_6$ in Figure S1 in the Supplementary Information. All four peaks of ${}^{11}\text{B}_2\text{H}_6$ are present in the spectrum of the as-deposited sample, and only the relative intensities of these four peaks change with temperature and the thermal history of the sample. This seems to suggest that there are at least two distinct matrix sites for B₂H₆ in solid pH₂, and the constant peak frequencies argue for homogeneous matrix sites where local crystal imperfections are minimal. After the B₂H₆/pH₂ crystal has been annealed, temperature changes result in population transfers between different matrix sites. The ν_8 spectrum also reflects an ensemble average over the same matrix site populations, but the linewidths of the individual transitions are much broader such that the changes in the ν_{8} lineshape with temperature are less evident. However, the ν_8 peak becomes significantly broader at 1.5 K compared to 4.0 K, and a secondary peak at $\sim 2608.8 \, \text{cm}^{-1}$ grows in intensity at low temperatures (see peak marked with asterisk in Fig. 4). The ν_{16} spectra in Fig. 4 show that the populations of B₂H₆ in different matrix sites are significantly altered over the 1.5 to 4.0 K temperature range. We observe similar reversible spectral changes for B₂D₆/pH₂ samples over the same temperature range. The origin of the broad lineshapes for ν_{13} and ν_{8} compared with the other B₂H₆ fundamentals is not known (homogeneous and inhomogeneous broadening) but we have detected evidence that the fine structure is due to different alignments of B2H6 in the pH2 matrix. We plan to study this further and will report our findings in a future paper.

3.3. Combination bands in B₂H₆ and B₂D₆

As discussed by Duncan and co-workers, the region between 1800 and 1900 cm $^{-1}$ for B_2H_6 shows a complex set of absorptions that were first studied at modest resolution (0.3 cm $^{-1}$) in both the gas and crystalline phases [32]. Later Lafferty and co-workers studied this same region for an isotopically enriched sample of $^{10}B_2H_6$ at room temperature with sub-Doppler resolution [63]. Both studies showed that surprisingly the strongest band in this region is the $\nu_5+\nu_{15}$ (b_{3u}) combination band

and not the ν_{13} (b_{1u}) fundamental (bridge BH stretch/ring deformation). Lafferty and co-workers [63] were able to obtain a precise set of experimental rovibrational energy levels for three vibrational states, the 13^1 fundamental and two combination states, 5^115^1 and 9^115^1 . However, given all the possible interactions with dark states, they were not able to reproduce a fraction of the observed transitions (especially within the ν_{13} and $\nu_5+\nu_{15}$ bands) to within experimental uncertainty. Duncan comments that while it is firmly established that a strong two-state Fermi resonance interaction exists between the ν_{13} fundamental and $\nu_9+\nu_{15}$ combination band, that an intense combination band at lower wavenumbers than the ν_{13} fundamental is an apparent b-type band (i.e., b_{2u}) [32]. However, an earlier polarized single crystal study of 11 B₂H₆ reveals the presence of a c-type band in this region, assigned to ν_{13} , and three a-type bands, but no type-b bands. We will see what the pH₂ MIS reveals about the spectrum in this region.

One of our reasons for studying diborane is to investigate how well the VCI calculations reproduce the combination band spectra and to use the simulated spectrum to assign bands that show significant perturbations. Shown in Fig. 5 is the spectrum of a B₂H₆/pH₂ sample in the 1800 to 2050 cm⁻¹ region. The ν_{13} fundamental and $\nu_{9}+\nu_{15}$ combination band both show "normal" boron isotopic shifts, and the wavenumbers and intensities of both bands are well reproduced by the VCI calculations. Thus, the VCI calculations do exceptionally well in modeling the strong Fermi resonance (W = 54.7 cm^{-1}) between the 13^1 and 9^115^1 excited states, most likely because the two unperturbed states are separated by a relatively large energy difference ($\Delta_0 = 22.5 \text{ cm}^{-1}$) such that small matrix shifts in the unperturbed vibrational levels do not lead to significant differences in the coupling strengths [31]. In addition, the $\nu_9 + \nu_{15}$ combination band is well isolated (see Fig. 5) and can only couple to vibrational states with $b_{1\mathrm{u}}$ symmetry which is the $v_{13}=1$ excited state. Thus, it appears that trapping B₂H₆ in a pH₂ matrix does not significantly perturb the Fermi interaction between these two states. Note that the btype Coriolis resonance between 5¹15¹ and 13¹, that is present in the gas phase spectra as identified by Lafferty [63], is not important in the MIS spectra because the molecule is non-rotating.

The stronger intensity peaks near 1850 cm⁻¹ in Fig. 5 appear at first

to be the normal boron isotopic shift pattern for a relatively strong band, but with one additional lone peak to lower wavenumbers (~1833 cm⁻¹). However, in this region the computed IR spectrum only has peaks with non-negligible intensities associated with the $\nu_5 + \nu_{15}$ ($b_{3\nu}$), $\nu_7 + \nu_{14}$ (b_{3u}) , and v_9+v_{12} (b_{3u}) combination bands, and two of these combination bands ($\nu_5 + \nu_{15}$ and $\nu_7 + \nu_{14}$) show significant boron isotopic shift anomalies (see Fig. 5). The features near 1850 cm⁻¹ result from a Darling-Dennison resonance between the 7¹14¹ and 5¹15¹ excited states such that each state is strongly mixed. For example, for both \$^{11}B_2H_6\$ and $^{11}B^{10}BH_{6}$ the lower energy combination state is 62.5 % – 65.9.2 % $\nu_7 + \nu_{14}$ and 27.1 % – 24.6 % $\nu_5 + \nu_{15}$, but for $^{10}\text{B}_2\text{H}_6$ these energy levels appear to flip with the lower combination state with 54.8 % $\nu_5 + \nu_{15}$ and 36.1 % $\nu_7 + \nu_{17}$ and the upper combination state with 53.6 % $\nu_7 + \nu_{14}$ and 37.0 % $\nu_5 + \nu_{15}$. As the percentages of the contributing configurations (Hartree products) to these two states are comparable, it is difficult to assign one combination band to $\nu_5 + \nu_{15}$ and the other to $\nu_7 + \nu_{14}$. This makes simulating the B_2H_6/pH_2 spectrum in this region very difficult because this mixing can be strongly influenced by small shifts in the vibrational frequencies of B2H6 caused by interactions with the pH2 matrix. We believe the reason for the discrepancy between the observed and calculated spectrum in this region is related to the fact that the VCI calculations are for the isolated B₂H₆ molecule, while the experimental data are for B₂H₆ trapped in solid pH₂. Even though the matrix shifts in solid pH2 are small (<1%), small shifts in frequencies of vibrational modes that are in resonance with one another can result in substantial differences between the computed spectrum and the experimental pH2 matrix isolation spectrum.

We suspect this is the case for the features around 1850 cm^{-1} . The $\nu_9+\nu_{12}$ combination band is calculated to have a somewhat "normal" boron isotopic splitting pattern; based on the VCI calculations the 9^112^1 excited state is not strongly coupled to the 5^115^1 or 7^114^1 states. However, when we examine the contributing configurations to the 5^115^1 and 7^114^1 VCI states, the two states have very similar percentages, and the dominant configuration switches in going from $^{11}B^{10}BH_6$ to $^{10}B_2H_6$. An energy level diagram from 1820 to 2020 cm $^{-1}$ of the excited vibrational states in this region for all three isotopologues of B_2H_6 is

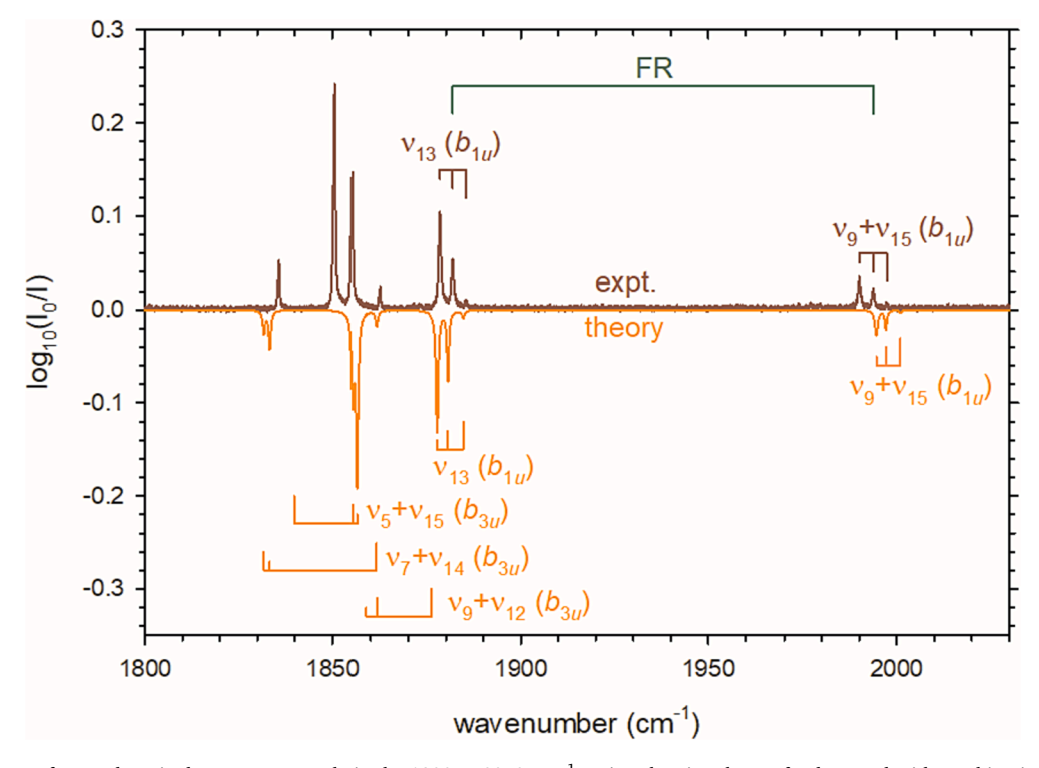


Fig. 5. Infrared spectra of an as-deposited B_2H_6/pH_2 sample in the 1800 to 2050 cm⁻¹ region showing the ν_{13} fundamental with combination bands at lower and higher wavenumbers. There is a strong Fermi resonance between 13^1 and 9^115^1 .

shown in Figure S2 in the Supplementary Information. The wavenumber difference between these two coupled states (Δ) is approximately 23 cm⁻¹, while the energy difference between the ν_{13} and $\nu_9 + \nu_{15}$ states involved in the strong Fermi resonance was 116 cm $^{-1}$, thus the $\nu_7 + \nu_{14}$ and $\nu_5 + \nu_{15}$ combination bands are much closer in energy and therefore more sensitive to small perturbations. While we make vibrational assignments for ν_{13} and $\nu_9+\nu_{15}$ based upon the VCI calculations, we hesitate to make vibrational assignments of the strong lines near $1850~\mathrm{cm}^{-1}$ simply because we cannot make a unique assignment. The computed spectrum gets the relative intensity values in this region qualitatively correct; it predicts the strongest band is the $\nu_5+\nu_{15}$ combination band, but the specific peak frequencies do not match the observed spectrum. Interestingly, even the high resolution (res = 0.0033 cm^{-1}) gas phase work of Lafferty and co-workers were unable to assign the $\nu_5 + \nu_{15}$ and ν_{13} bands to within experimental precision, and they attribute this to interactions with a larger number of dark states for $\nu_5 + \nu_{15}$ as compared to the $\nu_9 + \nu_{15}$ combination band, and because they were not able to establish a satisfactory resonance scheme [63].

There are a variety of combination bands and ¹⁰B¹¹BH₆ fundamental transitions observed in the region near the ν_8 fundamental. In Fig. 6 we show the region between 2540 and 2800 cm⁻¹ for the most concentrated B_2H_6/pH_2 sample (i.e., $[B_2H_6] = 58(1)$ ppm) that shows several weak combination bands. At this concentration, the ν_8 fundamental is off scale but the $\nu_5+\nu_6$ combination band is clearly observed. The computed spectrum predicts a Darling-Dennison coupling between v_5+v_6 (b_{2u}) and $2\nu_5 + \nu_9$ (b_{2u}) that produces the observed features that are assigned to the $\nu_5 + \nu_6$ combination band. The $\nu_5 + \nu_6$ combination band has not been reported previously in the gas phase likely because it is so close to the strong v_8 fundamental. The computed spectrum also predicts that the v_{11} (b_1) mode of ${}^{10}\mathrm{B}{}^{11}\mathrm{BH}_6$ is IR allowed and observed just below ν_8 . The weak intensity $\nu_3 + \nu_{17}$ (b_{3u}) combination band is well reproduced by the VCI calculations, and the computations reveal that this combination band is not involved with any strong resonances. However, both the $\nu_7 + \nu_{13}$ (b_{3u}) and $\nu_6 + \nu_{14}$ (b_{3u}) combination bands involve excited states that are resonantly coupled to three quanta excitations, $7^19^115^1$ and 5¹9¹14¹, respectively, and the predicted transitions do not quantitatively agree with the observed spectra. This again is likely due to the extreme sensitivity that strongly resonating states display to small pH2 matrix induced perturbations. The two peaks observed at $\sim 2571~\text{cm}^-$

are not predicted by the VCI calculations which were limited to only calculating two quanta combination bands. But the vibrational analysis of the 5^16^1 excited state showed a resonant coupling to the 5^29^1 excited state, and we can estimate the frequency and intensity of this three quanta combination band from this analysis. The results are shown in Fig. 6 where we assign the small peaks near 2571 cm⁻¹ to the $2\nu_5+\nu_9$ (b_{2u}) combination band. This emphasizes that to accurately predict the IR spectrum of diborane one needs to go beyond the double harmonic approximation to explain all the features in the observed spectra, and that the VCI calculations can quantitatively predict the observed pH₂ matrix isolation spectra for most features. Additional comparisons of the experimental and VCI calculated spectra are shown in Figures S3 – S5 in the Supplementary Information for $2\nu_{18}$, $\nu_3+\nu_{18}$, $\nu_4+\nu_{17}$, and $\nu_7+\nu_{17}$ for B_2H_6 and ν_3 of $^{11}B^{10}BH_6$.

Now let us explore further the level of agreement between the calculated and experimental spectrum for B₂D₆. Shown in Fig. 7 is the spectrum of a B_2D_6/pH_2 sample in the region of the ν_{13} fundamental and $\nu_0 + \nu_{15}$ combination band, which have been reported to be in a Fermi resonance [31,32]. Once again, the simulated spectrum reproduces the positions and intensities of both the ν_{13} and $\nu_{9}+\nu_{15}$ bands very well. The computed spectrum also reproduces the single overlapping feature observed for the $\nu_5 + \nu_{15}$ (b_{3u}) combination band at $\sim 1320 \text{ cm}^{-1}$ that shows almost no boron isotopic shifts (all three isotopologue peaks overlap). However, in the region between the assigned $\nu_9 + \nu_{15}$ combination band and ν_{13} fundamental, there are several absorption features that do not display the normal boron isotopic splitting pattern. There are multiple combination bands predicted in this region, v_7+v_{14} (b_{3u}), $\nu_9 + \nu_{12} (b_{3u}), \nu_4 + \nu_{14} (b_{1u}), \nu_4 + \nu_9 (b_{2u}), \nu_{14} + \nu_{15} (b_{2u})$ and three overtones of ${}^{11}B^{10}BD_6$, namely, $2\nu_{15}$ (a_1), $2\nu_{14}$ (a_1), and $2\nu_4$ (a_1). Two of the combination bands in this region, $\nu_7 + \nu_{14}$ (b_{3u}) and $\nu_9 + \nu_{12}$ (b_{3u}), carry most of the oscillator strength and the $\nu_7+\nu_{14}$ combination band is an interesting example of a two quanta excited state. For the 11B2D6 isotopologue, the 7¹14¹ excited state is relatively unperturbed (leading term = 0.9520), however, the $7^{1}14^{1}$ excited state for ${}^{11}B^{10}BD_{6}$ is only $36.9 \% \nu_7 + \nu_{14}$ and is coupled to $2\nu_{15}$ (12.8 %) and $2\nu_7$ (18.6 %). For $^{10}B_2D_6$ the 7^114^1 excited vibrational state is coupled to 9^112^1 via a Darling-Dennison resonance. This makes the assignment of the features between v_{13} and v_9+v_{15} rather difficult and instead we just compare the experimental and calculated spectra in this region by labeling the major

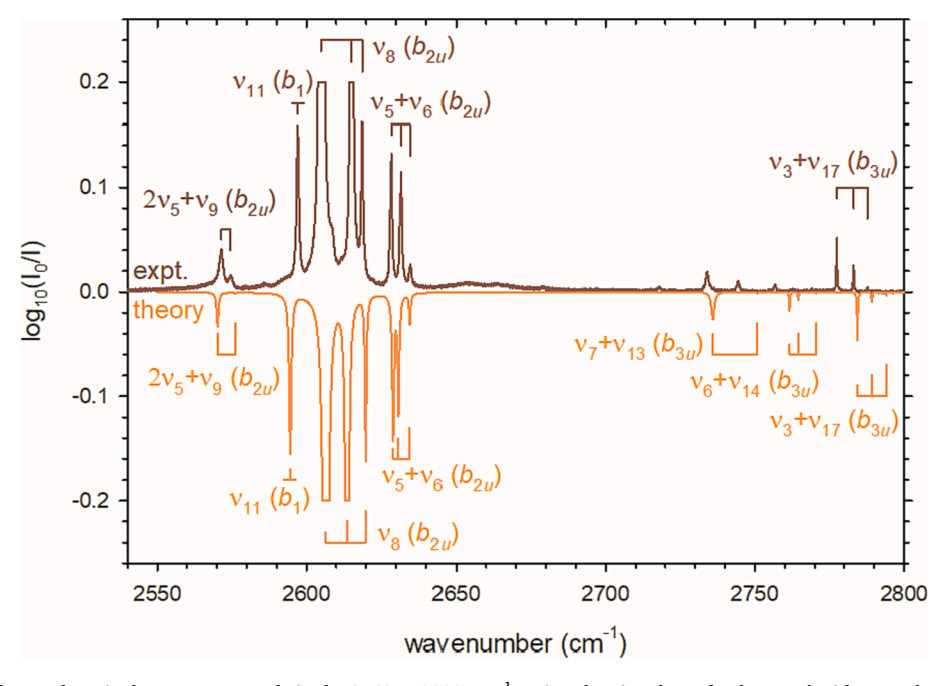


Fig. 6. Infrared spectra of an as-deposited B_2H_6/pH_2 sample in the 2540 to 2800 cm⁻¹ region showing the ν_8 fundamental with several combination bands at higher wavenumbers. Also note the single peak due to ν_{11} of $^{10}B^{11}BH_6$ that is weakly infrared active.

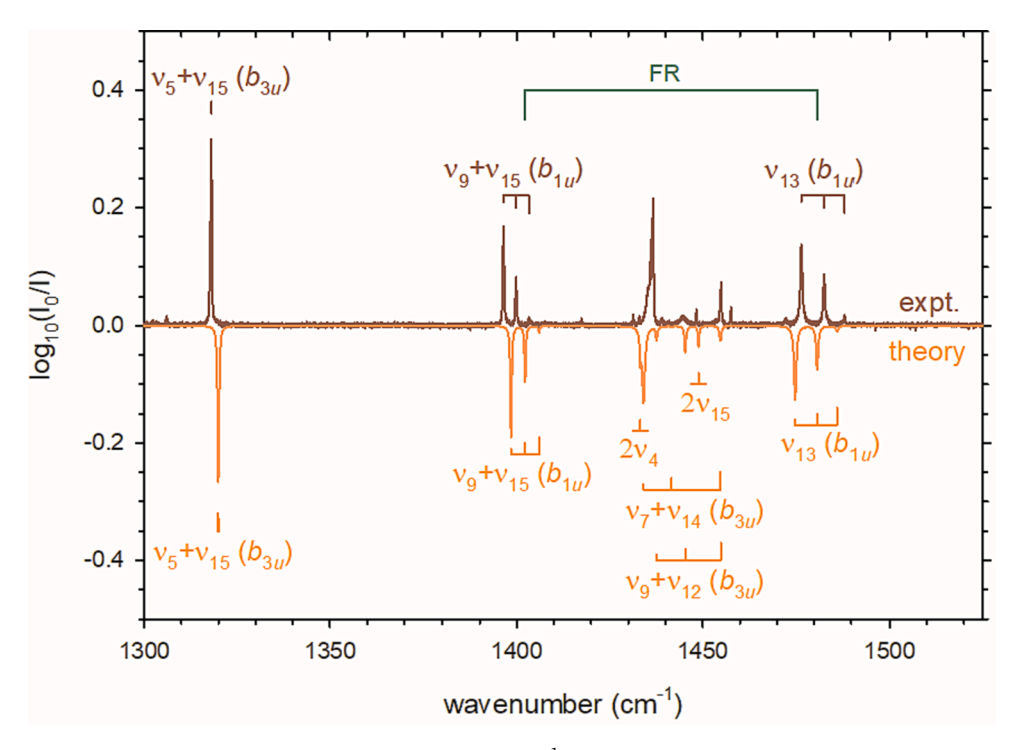


Fig. 7. Infrared spectra of an as-deposited B_2D_6/pH_2 sample in the 1300 to 1525 cm⁻¹ region showing the ν_{13} fundamental along with several combination bands. Like B_2H_6/pH_2 , there is a strong Fermi resonance between 13^1 and 9^115^1 .

peaks from the simulated spectrum. Like B_2H_6 , it appears that the calculated infrared spectrum for B_2D_6 reproduces the pH_2 MIS spectrum quantitatively except for certain regions where bands are extensively perturbed by Fermi and Darling-Dennison resonances.

The region around the ν_{16} and ν_{8} fundamentals of $B_{2}D_{6}/pH_{2}$ is another important region where the simulated spectrum does very well in reproducing the pH_{2} matrix isolation spectrum. Shown in Fig. 8 is the

1750 to 2050 cm⁻¹ region showing the ν_{16} and ν_{8} fundamentals of B₂D₆ for a relatively high concentration sample ([B₂D₆] = 123(4) ppm). As discussed earlier, both the ν_{16} and ν_{8} fundamentals are well reproduced by the calculated spectrum. In this spectral region the ν_{1} (a_{1}) and ν_{11} (b_{1}) vibrational modes for the ¹⁰B¹¹BD₆ isotopologue are also observed. Note that the ν_{1} vibration of ¹⁰B¹¹BD₆ has been reported to be in a Fermi resonance with $2\nu_{3}$ (a_{1}) [32], and we detect a peak for $2\nu_{3}$ at 1822.59

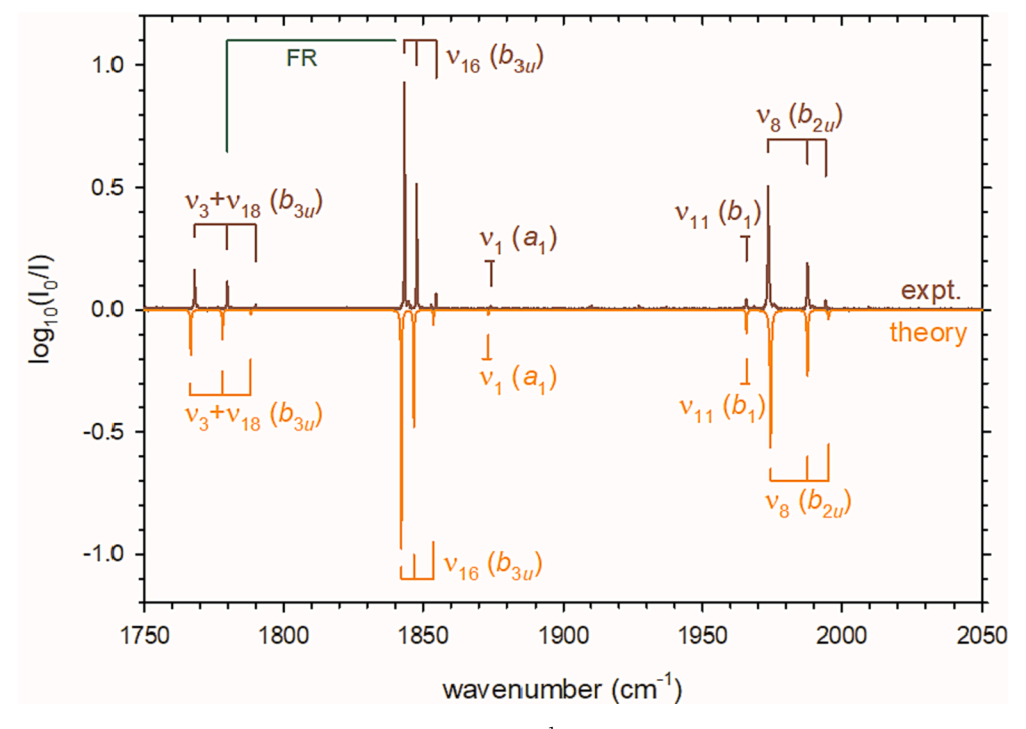


Fig. 8. Infrared spectra of an as-deposited B_2D_6/pH_2 sample in the 1750 to 2050 cm⁻¹ region showing the ν_{16} and ν_{8} fundamentals along with several combination bands. There is a strong Fermi resonance between the 16^1 and 3^118^1 vibrational states. Also note the single transitions due to ν_{1} and ν_{11} of $^{10}B^{11}BD_6$ that are weakly infrared active.

cm⁻¹ very close to the calculated peak position (1820.90 cm⁻¹), it is just not visible on the scale of Fig. 8. Finally, the v_3+v_{18} (b_{3u}) combination band is also observed in this region which has been previously assigned to a Fermi resonance with the ν_{16} mode of B_2D_6 [32]. The frequencies and intensities of the $\nu_3+\nu_{18}$ combination band are simulated well by the VCI calculations and investigation of the contributing configurations shows the Fermi resonance between $\nu_3+\nu_{18}$ and the ν_{16} fundamental. This Fermi resonance is most prominent in the ¹⁰B₂D₆ isotopologue as gauged by the steady increase in the intensity of the $\nu_3 + \nu_{18}$ combination band from 18.32 km/mol for $^{11}\text{B}_2\text{D}_6$ to 27.41 km/mol for $^{10}\text{B}_2\text{D}_6$. These types of two state Fermi resonances are well reproduced by the VCI calculations and suggest that these perturbations are less effected by matrix shifts than close lying states coupled by multiple Darling-Dennison resonances. Additional comparisons of the experimental and VCI calculated spectra are shown in Figures S6 and S7 in the Supplementary Information for $\nu_{12}+\nu_{17}$ of B_2D_6 and $2\nu_3$ of ${}^{11}B^{10}BD_6$.

In summary, the VCI calculations quantitatively reproduce the six observed vibrational fundamentals and many of the combination bands for both B2H6 and B2D6, however, in some regions where multiple combination bands overlap with the same excited state vibration symmetry, the VCI calculations do not reproduce the observed spectra quantitatively. We speculate that the cause of these discrepancies between the pH2 matrix isolation spectra and the VCI calculations is the pH2 matrix induced shifts that are not accounted for in the VCI calculations. When two states are strongly coupled via a Fermi resonance, it appears that matrix shifts in the vibrations caused by interactions with the pH₂ matrix do not significantly perturb the spectra such that the VCI calculations reproduce the pH2 matrix isolation spectra. However, in spectral regions where two or more excited sates are coupled by Darling-Dennison resonances, and that are energetically close together, then small shifts in the vibrational frequencies induced by the pH2 matrix can produce big changes in the resonant coupling such that the matrix spectra are not well reproduced by the VCI calculations.

4. Discussion

4.1. Matrix shifts and mean absolute errors

Jacox has shown that matrix shifts are smallest for neon matrices and increase with increasing atomic mass of the noble gas atom due to the increase in the van der Waals forces going down the periodic table [12,13]. Matrix shifts originate from the difference in the solvation energy for the molecule in the ground and v=1 excited vibrational states. For example, if the excited state has a greater solvation energy than the ground vibrational state, then the vibrational frequency of the matrix isolated species is lowered relative to its gas phase value. Based solely on the precise noble gas and pH₂ (isotropic) pair potentials, one would expect the pH₂ matrix shifts to be comparable to a Ne matrix, and smaller than Ar matrix shifts. However, while the pair potentials for Ne and pH₂ are very similar, the lattice constant (intermolecular/atomic distance) for the pH₂ crystal (3.79 Å) is consider baly larger than that of Ne (3.16 Å) due to quantum effects. It therefore is informative to compare the vibrational frequencies measured for ¹¹B₂H₆ in pH₂ with the analogous values measured for Ne and Ar matrices [23,64]. The measured matrix shifts for five infrared active vibrational modes of ¹¹B₂H₆ are presented in Table 5 and plotted in Fig. 9 as a bar chart (note: the v_{13} peak position was not published for an Ar matrix). The measured peak wavenumbers used to calculate the matrix shifts reported in Table 5 are presented in Table S9 in the Supplementary Information. As can be seen in Fig. 9, the pH2 matrix shifts typically fall in between the Ne and Ar values with the Ar matrix producing the greatest red shifts, and the Ne matrix with the greatest blue shifts. This can be rationalized by thinking about the lattice size for a single substitution lattice site in the different matrices and the balance between attractive and repulsive intermolecular forces. The Ar lattice has a nearest neighbor spacing [65] of 3.76 Å and the deepest intermolecular potential ($D_e = 99.5 \text{ cm}^{-1}$ and

Table 5Matrix shifts for five IR-active modes of ¹¹B₂H₆ trapped in Ne, pH₂, and Ar.

Mode	Ne shift ^a	pH ₂ shift	Ar shift ^b	VCI ^c
ν_{14}	1.85	-0.78	1.40	-0.60
ν_{18}	-0.09	-3.03	-4.29	-3.63
ν_{17}	-5.09	-6.02	-10.72	1.12
ν_{16}	2.12	-2.67	-2.85	-2.68
ν_8	1.77	-3.92	-5.85	-2.36
AVG.	0.11	-3.28	-4.46	-1.63
MAE	2.18	3.28	5.02	1.73
MAX	-5.09	-6.02	-10.72	-3.63

^a Ref. [23].

 $R_e = 3.76 \text{ Å}$) [66] of the three matrices and therefore in general, the Ar matrix produces the greatest redshifts in guest vibrations. In contrast, the Ne matrix has a smaller nearest neighbor spacing (3.16 Å) [65] and a smaller binding energy ($D_e = 29.4 \text{ cm}^{-1}$ and $R_e = 3.08 \text{ Å}$) [66] such that three of the five vibrational modes of ¹¹B₂H₆ are blue shifted relative to the gas phase frequency. The pH2 matrix shifts usually fall in between the shifts measured for Ne and Ar; this is due to a combination of the large nearest neighbor spacing for solid pH2 and the weak intermolecular forces [41]. In quantum solids the guest species occupy a volume related to the amplitude of the zero-point motion, not the hard-sphere diameter. The quantum crystal can lower its total energy by expanding, reducing the kinetic energy of localization at the cost of reducing the potential energy contributions to the total energy. Note that the binding energy and equilibrium bond length ($D_e = 25.7 \text{ cm}^{-1}$ and $R_e =$ 3.28 Å) [41] of the pair potential for pH_2 are comparable to the Ne values, but due to the lighter mass of H2 relative to Ne, the lattice spacing in the pH₂ quantum crystal is 20 % larger than Ne.

The ν_{17} mode shows the greatest matrix shifts of the five vibrations, which makes sense because this mode involves the bridged BH bonds that are highly anharmonic and this mode is the strongest intensity mode (e.g., ~400 km/mol), meaning that the transition dipole is the largest and thus this mode produces the greatest difference in the interaction of ${}^{11}B_2H_6$ ($\nu_{17}=0$) and ($\nu_{17}=1$) with the pH₂ matrix host. Attractive interactions in the $v_{17} = 1$ excited state must dominate for this mode since in all three matrices this mode is redshifted from its gas phase value and the redshift increases from going from Ne to pH2 to Ar. Similarly, the v_{18} mode (terminal BH antisymmetric deformation) displays redshifts in all three matrices and the matrix shift in Ne is almost zero due presumably to greater repulsive interactions in Ne matrices. The two high frequency terminal BH bond vibrations (ν_{16} and ν_{8}) both produce redshifts in pH2 and Ar, but are blue shifted in Ne. Finally, the v_{14} vibration (terminal BH in-plane wag) displays blue shifts in Ne and Ar, but a small redshift in solid pH2. This again can be rationalized by the lack of strong repulsive intermolecular interactions in the "soft" quantum crystal composed of light pH2 molecules that are inflated by zeropoint motion.

To make quantitative comparisons of the pH_2 matrix isolation spectra with accurate anharmonic vibrational calculations for the isolated molecule, we must account for these matrix shifts. We can treat the matrix shifts as errors in the isolated molecule's vibrational frequencies and convert them to mean absolute errors (MAE) of the vibrational frequencies. For the five $^{11}B_2H_6$ vibrations presented in Table 5, the MAE equals 2.13, 3.29, and 5.02 cm $^{-1}$ for Ne, pH $_2$, and Ar matrices, respectively. Thus, the Ne matrix spectroscopic data have a smaller MAE than the pH $_2$ matrix results for these specific vibrational modes. This again likely results from greater repulsive intermolecular interactions in Ne matrices that counter act the attractive interactions leading to smaller net changes, and thus in this respect, the Ne matrix results represent the smallest errors with respect to the gas phase results. Furthermore, the results in Ne show both redshifts and blue shifts, while typically in pH $_2$ and Ar matrices, the vibrations of a guest species are

^b Ref. [64].

^c Matrix shifts calculated as $\Delta \nu = \nu_{VCI} - \nu_{gas}$.

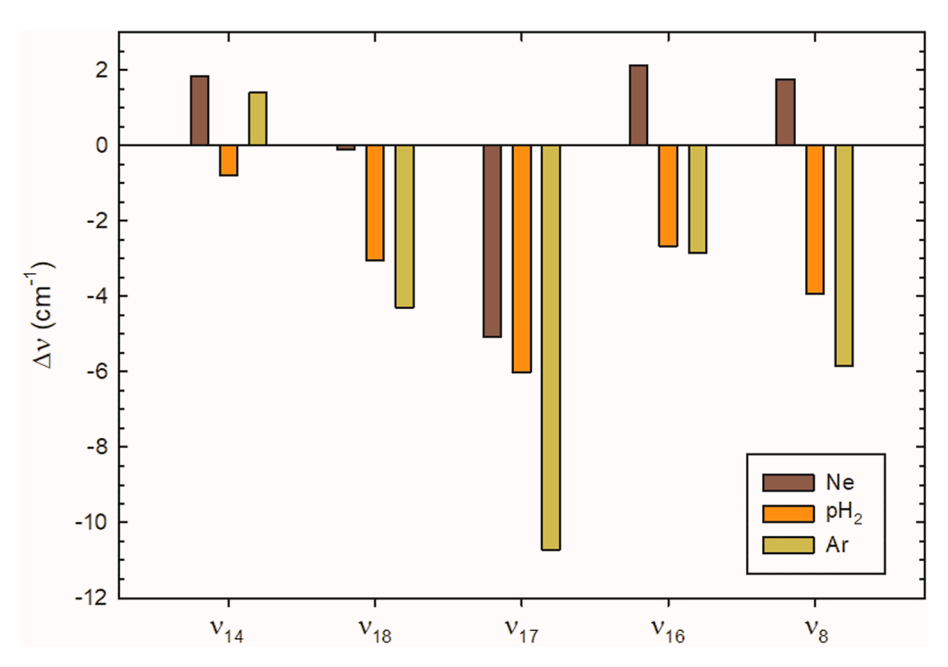


Fig. 9. Comparison of the experimental matrix shifts for five IR-active fundamental vibrational modes of ¹¹B₂H₆ isolated in Ne, pH₂, and Ar matrices.

redshifted leading to systematic deviations from the gas phase values. Nonetheless, all three matrices produce reasonably small MAEs (2–5 \mbox{cm}^{-1}) that are approaching spectroscopic accuracy (<1 \mbox{cm}^{-1}) suggesting that Ne and pH $_2$ matrix isolation, and even Ar matrix isolation, can be used to test the accuracy of anharmonic vibrational calculations on high quality PESs.

To further quantify how pH₂ matrix isolation spectroscopic results compare to highly accurate anharmonic vibrational calculations, we first must assess how the current anharmonic calculations reproduce the five vibrations with the available high-resolution gas phase results. For the five vibrations presented in Table 5, the MAE is 1.73 cm⁻¹ for a comparison of the current VCI calculations with available high resolution gas phase data ($\Delta \nu = \nu_{\rm theory} - \nu_{\rm gas}$). Thus, while this just falls short of so-called spectroscopic accuracy, it is remarkably good for an eight atom species with highly anharmonic three-center two-electron banana bonds. Furthermore, this level of accuracy is comparable with the matrix shift errors presented above, and thus MIS can be used to test anharmonic vibrational calculations at nearly spectroscopic accuracy. The matrix shifts produced in Ne and pH2 matrices are comparable to the level of agreement between the anharmonic vibrational calculations and the gas phase vibrational origins. As demonstrated in this study, it is much easier to measure the vibrational frequencies using MIS than room temperature gas phase measurements where rovibrational bands overlap extensively and the full rovibrational spectrum must be analyzed to get the band origin. Even the Ar matrix results with a MAE of 5.02 cm⁻ can be used to test anharmonic vibrational calculations, although both pH₂ and Ne are slightly better for this task. In terms of differences between Ne and pH2 matrix isolation results, the Ne matrices produce smaller MAEs, but the challenge is to assign spectra with significant matrix splitting's. That is, the IR spectra of B₂H₆ dispersed in Ne matrices typically shows more matrix site effects than pH2 matrices, for example the three peak boron isotopic splitting pattern is frequently doubled or tripled by so-called matrix site splitting's in the Ne matrix isolation spectra [23]. Further, typically these multiple matrix sites cannot be annealed away easily in the Ne matrices. While as we have shown pH2 matrices are not immune to matrix site splitting's, the site splitting's in pH2 are usually smaller than in Ne matrices, and thus their importance is diminished.

We now compare the fundamental frequencies predicted by the anharmonic vibrational calculations with the pH_2 matrix isolation

spectroscopic data to evaluate how well theory reproduces experiment. For each isotopologue we calculate the MAEs using the six pH2 matrix isolation fundamental frequencies measured in this study, with three additional peaks (ν_1 , ν_3 , and ν_{11}) for $^{10}B^{11}BH_6$. Based upon the current studies of B_2H_6 isolated in solid pH_2 , we can achieve MAEs of 1.70, 2.41, and 1.88 cm^{-1} for ${}^{11}\text{B}_2\text{H}_6$, ${}^{10}\text{B}^{11}\text{B}\text{H}_6$, and ${}^{10}\text{B}_2\text{H}_6$, respectively, using the six fundamental vibrations measured for each isotopologue. Such small MAEs are the direct result of the accuracy of the anharmonic vibrational calculations and the fact that the pH2 matrix isolation frequencies are comparable to the gas phase frequencies at this level of scrutiny (small matrix shifts). This confirms that pH2 matrix isolation spectroscopy can be used to validate or test anharmonic vibrational calculations and only if accuracies greater than 5 cm⁻¹ are required should gas phase results be needed. The B₂D₆ spectroscopic results are analogous with MAEs of 1.55, 1.29, and 1.48 cm⁻¹ for the ${}^{11}B_2D_6$, ${}^{10}B_1{}^{11}BD_6$, and ${}^{10}B_2D_6$, respectively, where these values are even slightly lower due to the reduction in the vibrational frequencies for the heavier isotopologue. Note that nine fundamental frequencies were compared for \$\frac{11}{11}B^{10}BD_6\$ while only six for ${}^{11}B_2D_6$ and ${}^{10}B_2D_6$, analogous to B_2H_6 .

As expected, the MAEs for the two-quanta combination bands and overtones are larger due presumably to the greater uncertainties in the calculated values. The MAEs for six (seven for $^{11}B^{10}BH_6$) combination bands and overtones measured for B_2H_6 are 4.91, 3.28, and 3.62 cm $^{-1}$ for $^{11}B_2H_6$, $^{10}B^{11}BH_6$, and $^{10}B_2H_6$, respectively. Thus, it appears that the errors approximately double for the combination bands that necessarily include contributions from two vibrational modes. These MAEs do not include the combination bands where a unique assignment is not possible, thus the errors increase even more for some combination bands that access strongly resonating vibrational states. A similar increase in the MAEs for combination bands compared to fundamentals is observed for B_2D_6 , specifically, 2.34, 2.20, and 3.04 cm $^{-1}$ for $^{11}B_2D_6$, $^{10}B^{11}BD_6$, and $^{10}B_2D_6$, respectively, based on four combination bands for $^{11}B_2D_6$ and $^{10}B_2D_6$ and five states (one extra $2\nu_3$ overtone) for $^{11}B^{10}BD_6$.

4.2. Probing anharmonic resonance polyads with matrix isolation IR spectra

As discussed earlier, trapping a molecule in a pH₂ matrix necessarily produces relatively small shifts in the vibrational fundamentals of a trapped species such that typically an experimental pH₂ matrix isolation

spectrum of a guest molecule can be assigned within the double harmonic approximation using harmonic vibrational frequencies with scaling factors and harmonic intensities. However, in the case of molecules such as diborane that have multiple Fermi and Darling-Dennison anharmonic resonances, there can be additional infrared absorptions that cannot be rationalized using the double harmonic approximation, and instead a fully anharmonic vibrational analysis must be performed. Even then in some spectral regions where there are anharmonic resonance polyads, small matrix shifts (<10 cm⁻¹) in the vibrational frequencies can lead to significant changes in the relative intensities and positions of bands in the matrix isolation spectrum. In these spectral regions in which anharmonic resonance polyads are expected to be important, for example the region between 1800 and 1900 cm⁻¹ in B₂H₆ and 1400 to 1500 cm^{-1} in B_2D_6 , we expect that the matrix isolation spectrum to have different frequencies and intensities than the gas phase spectrum, because these regions are uniquely sensitive to matrix shifts. Furthermore, the three isotopologues of diborane (B₂H₆ or B₂D₆) experience different anharmonic couplings such that in these regions you lose the three peak normal boron isotopic splitting pattern with the ¹¹B₂H₆ features at lowest wavenumbers with the greatest intensity and the ¹⁰B₂H₆ features at the highest wavenumbers with the lowest intensity. It then becomes very difficult to make one-to-one assignments.

Our comparison of the VCI calculated infrared spectrum with the pH₂ matrix isolation spectra showed that these computational methods that intrinsically treat the Fermi and Darling-Dennison resonances can reproduce the vibrational fundamentals, several combination bands, and many Fermi resonances within the spectrum. The exception is in regions where multiple vibrational states are coupled by anharmonic resonances. As we have stated, we believe the disagreement in these localized spectral regions is due to matrix perturbations which can have large effects on these types of anharmonic resonance polyads because even small shifts on the order of 5–10 cm⁻¹ can manifest in bright/dark states being tuned into or out of resonance. What is still unproven is whether the discrepancy between the calculated and experimental spectra in these regions would go away if we could record the MIS spectrum in a matrix that produced no matrix shifts. In other words, we assume that the discrepancy is caused by the fact that the calculated spectrum is for the isolated gas phase molecule, whereas the experimental spectrum was recorded with diborane trapped in solid pH₂.

Obviously, there is no matrix host that produces zero matrix shifts, but trapping a guest species in solid neon or liquid helium nanodroplets are both known to produce very small matrix shifts. We have discussed MIS using neon as a host, but another possibility is to trap a molecule in a liquid helium nanodroplet. In fact, Pullen et al. published a paper in 2018 on the infrared spectroscopy of propene (CH3CHCH2) isolated in both solid pH2 and in helium nanodroplets (HENDI) [67]. This paper also focused on the role of matrix shifts in the analysis of anharmonic resonances. In this work they investigate the region between 2800 and 3100 cm⁻¹, in which six C—H stretch fundamentals and the overtone of the γ -CH₃ antisymmetric bend have been assigned in the gas phase. However, upon cooling propene to less than 0.4 K in liquid helium nanodroplets, the spectrum contains 26 resolved vibrational bands emphasizing the importance of anharmonic resonances [67]. By comparing the HENDI spectra with the available gas phase measurements, they find the HENDI spectra have an average red shift of 1.7 \pm $0.8~\text{cm}^{-1}$ and the pH $_2$ MIS spectra have an average red shift of 4.4 ± 1.9 cm⁻¹. Thus, trapping a guest molecule in a liquid helium nanodroplet could better approximate the zero matrix shift environment needed to study anharmonic resonances in more detail. Like what we have found for diborane, only in certain regions, e.g., 2920–2950 cm⁻¹, that involve heavily mixed modes do they find discrepancies between the gas phase and HENDI spectra. They showed that in general the HENDI and pH₂ MIS spectra are qualitatively similar, but in two localized regions the spectrum exhibits qualitatively different behavior depending upon the host environment. This is not surprising, and studying the response of Fermi resonances to changes in isotopic substitution, pressure

variations, or different solvent environments are all established ways to probe anharmonic resonances [68]. They also used a simplified two-state interaction model to show that 10 cm^{-1} shifts in the unperturbed frequencies can lead to qualitative changes in the observed spectra. This is all consistent with what we have measured for diborane trapped in solid pH₂, and it would be interesting to try to incorporate matrix shifts into the VCI calculations by trying to include intermolecular interactions with the surrounding pH₂ matrix to test these ideas [69].

One of Duncan's goals in his extensive spectroscopic investigations of diborane was to determine a physically realistic and numerically precise harmonic potential energy function for diborane [31]. Such a potential can be used to make predictions of the Coriolis coupling constants between fundamentals in the fully symmetric isotopologues, to predict the harmonic contributions to the vibration–rotation constants for all vibrations, and in the analysis of the Fermi resonances between ν_{13} and $\nu_9 + \nu_{15}$ in all species, and between ν_1 and $2\nu_3$ and ν_{16} and $\nu_3 + \nu_{18}$ in B₂D₆. Duncan developed the diborane potential in 1983 well before the types of anharmonic vibrational calculations presented here for high quality ab initio potential functions were possible. Duncan therefore used the derived empirical potential to estimate the harmonic and anharmonic contributions to each vibrational mode, so that they could perform a Fermi analysis to quantify the effects of these resonant perturbations. Nowadays using the VCI calculations that explicitly treat the Fermi and Darling-Dennison anharmonic couplings, we avoid all the approximations Duncan necessarily had to employ to develop his empirical potential. The discrepancies with the earlier work of Duncan and coworkers are therefore related to the difficulty in determining the harmonic and anharmonic contributions to the fundamental vibrations of B₂H₆.

Based on our infrared studies of B2H6 and B2D6 in solid pH2, along with the anharmonic vibrational calculations that allow the highresolution spectrum to be simulated, we now feel confident that anharmonic vibrational calculations are capable of reproducing all the diborane fundamental vibrational frequencies and intensities to within experimental uncertainties (matrix shifts) and that the anharmonic vibrational frequencies in Tables 3 and 4 are more accurate than the current values presented in the NIST webbook [62]. By comparing the predictions for the six infrared active fundamentals with the pH₂ data, we confirm that the simulated spectrum reproduces the observed fundamentals to within $5\ \mathrm{cm}^{-1}$. We therefore speculate that the vibrational frequencies and intensities predicted here for B₂H₆ and B₂D₆ (including the non-centrosymmetric isotopologues) are the most accurate values reported to date. Indeed, the accuracy of these anharmonic vibrational calculations could be tested further by performing experiments on partially deuterated samples to see if the calculations predict the peak frequencies accurately for the most intense absorption features of B₂D₄H₂, for example.

5. Conclusions

The infrared spectrum of B₂H₆ was instrumental in determining the bridge structure of diborane that involves two bridging and four terminal BH bonds. After this bridge structure was established, the fundamental vibrational modes of B2H6 and B2D6 were extensively studied both by spectroscopists and theoreticians as a prototype of electron-deficient molecules. It could be argued that the reason such large discrepancies between experiment and theory on the fundamental vibrational frequencies of diborane persisted for so long is directly related to the presence of the three-center, two-electron banana bonds. The early spectroscopic works suffered from poor spectral resolution which is necessary to fully resolve the rovibrational bands of B2H6 and B₂D₆ to determine precise ground state constants for the three naturally abundant diborane isotopologues. But even more importantly, a theoretical description of the anharmonic vibrational dynamics would require advances in both electronic structure calculations of the PES of polyatomic systems as well as calculations of the nuclear dynamics on

those PESs.

In this paper, we present pH2 matrix isolation infrared spectroscopic measurements of all three isotopologues of B₂H₆ and B₂D₆ to determine precise vibrational frequencies of six of the eight infrared active vibrational modes. In addition, we have the required sensitivity to detect several combination bands involving Fermi resonances with fundamentals. We wanted to ask the question: how well do modern theoretical approaches reproduce the anharmonic vibration dynamics of B₂H₆? To do this, we needed new highly accurate anharmonic vibrational calculations to be performed on all three naturally abundant isotopologues of both B2H6 and B2D6. As we show in this work, the VCI calculations reproduce the frequencies and intensities of the six infrared active fundamentals of both B_2H_6 and B_2D_6 very well, producing isotopically averaged MAEs equal to 2.00 cm⁻¹ and 1.44 cm⁻¹ for B₂H₆ and B₂D₆, respectively. We find that several combination bands, either produced in two-state Fermi resonances or simply by anharmonic couplings, are also well reproduced except with slightly larger MAE values. However, in some regions of the spectrum where several excited vibrational states are grouped together in the same energy region and have the same vibrational symmetry, the computed spectrum can reproduce the experimental spectrum qualitatively but not quantitatively. In these cases, it is still unclear whether this is a limitation of the anharmonic vibrational calculations or rather due to perturbations induced by the pH2 matrix which alter the anharmonic couplings, but conventional wisdom is leaning toward the matrix induced perturbations as the cause based on the available spectroscopic data. Nonetheless, the agreement between the pH2 matrix isolation results and the VCI computed infrared spectrum (frequencies and intensities) is remarkably good and we believe that the calculated vibrational fundamentals for all six isotopologues of diborane presented here represent the most accurate description of the vibrational dynamics of diborane published to date.

CRediT authorship contribution statement

Aaron I. Strom: Investigation. **Ibrahim Muddasser:** Investigation. **Guntram Rauhut:** Formal analysis, Software, Writing – review & editing. **David T. Anderson:** Conceptualization, Data curation, Formal analysis, Funding acquisition, Project administration, Resources, Supervision, Writing – original draft.

Declaration of competing interest

The authors declare that they have no known competing financial interests or personal relationships that could have appeared to influence the work reported in this paper.

Data availability

Data will be made available on request.

Acknowledgements

We want to thank University of Wyoming undergraduates Jordan J. Klaassen, Jennifer Gehred, and Adriauna Butler for their assistance in performing some of the first experiments on B_2H_6 isolated in solid pH_2 . This work was sponsored, in part, by the Chemistry Division of the U.S. National Science Foundation (grant no. CHE-2101719).

Appendix A. Supplementary data

Supplementary data to this article can be found online at https://doi.org/10.1016/j.jms.2024.111887.

References

- E. Whittle, D.A. Dows, G.C. Pimentel, Matrix isolation method for experimental study of unstable species, J. Chem. Phys. 22 (11) (1954) 1943.
- [2] H.E. Hallam, Vibrational Spectroscopy of Trapped Species, John Wiley, New York, 1973
- [3] S. Cradock, A. Hinchcliffe, Matrix Isolation, Cambridge University Press, Cambridge, 1975.
- [4] L. Andrews, M. Moskovits, Chemistry and Physics of Matrix-Isolated Species, Elsevier Science Publishers, Amsterdam, 1989.
- [5] M.E. Jacox, The spectroscopy of molecular reaction intermediates trapped in the solid rare gases. Chem. Soc. Rev. 31 (2) (2002) 108–115.
- [6] M.E. Jacox, On Walking in the Footprints of Giants, Annu. Rev. Phys. Chem. 61 (2010) 1–18.
- [7] E.B. Wilson Jr., J.C. Decius, P.C. Cross, Molecular Vibrations, Dover Publications Inc. New York, 1955.
- [8] D.J. Nesbitt, High-resolution infrared spectroscopy of weakly bound molecular complexes. Chem. Rev. 88 (6) (1988) 843–870.
- [9] S. Erfort, M. Tschöpe, G. Rauhut, Toward a fully automated calculation of rovibrational infrared intensities for semi-rigid polyatomic molecules, J. Chem. Phys. 152 (24) (2020).
- [10] M. Tschöpe, B. Schroder, S. Erfort, G. Rauhut, High-Level Rovibrational Calculations on Ketenimine, Front. Chem. 8 (2021).
- [11] D.F. Dinu, M. Podewitz, H. Grothe, T. Loerting, K.R. Liedl, On the synergy of matrix-isolation infrared spectroscopy and vibrational configuration interaction computations, Theor. Chem. Acc. 139 (12) (2020).
- [12] M.E. Jacox, Comparison of the ground-state vibrational fundamentals of diatomic -molecules in the gas-phase and in inert solid matrices, J. Mol. Spectrosc. 113 (2) (1985) 286–301.
- [13] M.E. Jacox, The vibrational-energy levels of small transient molecules isolated in neon and argon matrices, Chem. Phys. 189 (2) (1994) 149–170.
- [14] J.M. Bowman, K. Christoffel, F. Tobin, Application of SCF-CI theory to vibrational motion in polyatomic molecules, J. Phys. Chem. 83 (8) (1979) 905–912.
- [15] K.M. Christoffel, J.M. Bowman, Investigations of self-consistent field, SCF CI and virtual state configuration interaction vibrational energies for a model three-mode system, Chem. Phys. Lett. 85 (2) (1982) 220–224.
- [16] S. Carter, J.M. Bowman, N.C. Handy, Extensions and tests of "multimode": a code to obtain accurate vibration/rotation energies of many-mode molecules, Theor. Chem. Acc. 100 (1–4) (1998) 191–198.
- [17] M. Neff, G. Rauhut, Toward large scale vibrational configuration interaction calculations, J. Chem. Phys. 131 (12) (2009).
- [18] M.E. Fajardo, Matrix Isolation Spectroscopy in Solid Parahydrogen: A Primer, Pan Stanford Publishing Pte Ltd, Singapore, 2011.
- [19] M.E. Fajardo, Solid parahydrogen thickness revisited, Appl. Spectrosc. 73 (12) (2019) 1403–1408.
- [20] I. Muddasser, A.H.M. Nguyen, A.I. Strom, A.M. Hardee, B.G. Pluid, D.T. Anderson, Infrared spectroscopic studies of oxygen atom quantum diffusion in solid parahydrogen, J. Phys. Chem. A 127 (2023) 2751–2764.
- [21] S. Tam, M.E. Fajardo, Ortho/Para hydrogen converter for rapid deposition matrix isolation spectroscopy, Rev. Sci. Instrum. 70 (1999) 1926–1932.
- [22] B. Ziegler, G. Rauhut, Accurate vibrational configuration interaction calculations on diborane and its isotopologues, J. Phys. Chem. A 123 (15) (2019) 3367–3373.
- [23] Y.C. Peng, S.L. Chou, J.I. Lo, M.Y. Lin, H.C. Lu, B.M. Cheng, J.F. Ogilvie, Infrared and ultraviolet spectra of diborane(6): B2H6 and B2D6, J. Phys. Chem. A 120 (28) (2016) 5562–5572.
- [24] F. Stitt, Infra-red and Raman spectra of polyatomic molecules XV. Diborane, J. Chem. Phys. 9 (11) (1941) 780–785.
- [25] T.F. Anderson, A.B. Burg, The Raman spectrum of liquid diborane, J. Chem. Phys. 6 (10) (1938) 586–591.
- [26] R.P. Bell, H.C. Longuet-Higgins, The normal vibrations of bridged X₂Y₆ molecules, Proc. Roy. Soc. 183 (A995) (1945) 0357–0374.
- [27] W.C. Price, The structure of diborane, J. Chem. Phys. 15 (8) (1947) 614-615.
- [28] W.C. Price, The absorption spectrum of diborane, J. Chem. Phys. 16 (9) (1948) 894–902.
- [29] W.J. Lafferty, A.G. Maki, T.D. Coyle, High resolution infrared spectrum and structure of diborane, J. Mol. Spectrosc. 33 (2) (1970) 345–367.
- [30] J.L. Duncan, J. Harper, The structure of the diborane molecule, Mol. Phys. 51 (2) (1984) 371–380
- [31] J.L. Duncan, J. Harper, E. Hamilton, G.D. Nivellini, The empirical harmonic potential function of diborane, J. Mol. Spectrosc. 102 (2) (1983) 416–440.
- [32] J.L. Duncan, D.C. McKean, I. Torto, G.D. Nivellini, Diborane Infrared spectra of gaseous and crystalline phases, and a complete vibrational assignment, J. Mol. Spectrosc. 85 (1) (1981) 16–39.
- [33] E. Hamilton, J.L. Duncan, Diborane High resolution infrared rovibration studies of ¹⁰B₂H₆, J. Mol. Spectrosc. 90 (1) (1981) 129–138.
- [34] E. Hamilton, J.L. Duncan, Diborane High resolution infrared rovibration studies of ¹⁰B₂D₆, J. Mol. Spectrosc. 90 (2) (1981) 517–530.
- [35] J. Harper, J.L. Duncan, Diborane High-resolution infrared rovibration studies of $^{11}B_2H_6$ and $^{11}B_2D_6$, J. Mol. Spectrosc. 100 (2) (1983) 343–357.
- [36] J.F. Stanton, J. Gauss, Anharmonicity in the ring stretching modes of diborane, J. Chem. Phys. 108 (22) (1998) 9218–9220.
- [37] D. Begue, C. Pouchan, J.C. Guillemin, A. Benidar, Anharmonic treatment of vibrational resonance polyads-the diborane: a critical case for numerical methods, Theor. Chem. Acc. 131 (3) (2012).
- [38] L.O. Paulson, D.T. Anderson, High-resolution vibrational spectroscopy of transformic acid in solid parahydrogen, J. Phys. Chem. A 113 (9) (2009) 1770–1778.

- [39] L.O. Paulson, D.T. Anderson, Infrared spectroscopy of the amide I mode of N-methylacetamide in solid hydrogen at 2–4 K, J. Phys. Chem. B 115 (46) (2011) 13659–13667
- [40] M.E. Fajardo, S. Tam, Rapid vapor deposition of millimeters thick optically transparent parahydrogen solids for matrix isolation spectroscopy, J. Chem. Phys. 108 (1998) 4237–4241.
- [41] I.F. Silvera, The solid molecular hydrogens in the condensed phase Fundamentals and static properties, Rev. Mod. Phys. 52 (2) (1980) 393–452.
- [42] M.E. Fajardo, High-resolution rovibrational spectroscopy of carbon monoxide isotopologues isolated in solid parahydrogen, J. Phys. Chem. A 117 (50) (2013) 13504–13512.
- [43] M.E. Fajardo, C.M. Lindsay, Crystal field splitting of rovibrational transitions of water monomers isolated in solid parahydrogen, J. Chem. Phys. 128 (2008) 014505-1.
- [44] M.E. Fajardo, C.M. Lindsay, T. Momose, Crystal field theory analysis of rovibrational spectra of carbon monoxide monomers isolated in solid parahydrogen, J. Chem. Phys. 130 (2009) 244508-1–244508-10.
- [45] M.E. Fajardo, S. Tam, M.E. DeRose, Matrix isolation spectroscopy of H₂O, D₂O, and HDO in solid parahydrogen, J. Mol. Struct. 685–696 (2004) 111–127.
- [46] P.L. Raston, S.C. Kettwich, D.T. Anderson, High-resolution infrared spectroscopy of atomic bromine in solid parahydrogen and orthodeuterium, J. Chem. Phys. 139 (2013) 134304-1–134304-10.
- [47] A.I. Strom, K.L. Fillmore, D.T. Anderson, Hydrogen atom catalyzed ortho-to-para conversion in solid molecular hydrogen, Low Temp. Phys. 45 (6) (2019) 676–688.
- [48] F.M. Mutunga, K.M. Olenyik, A.I. Strom, D.T. Anderson, Hydrogen atom quantum diffusion in solid parahydrogen: The H + N2O → cis-HNNO → trans-HNNO reaction, J. Chem. Phys. 154 (2021) 014302.
- [49] T.B. Adler, G. Knizia, H.J. Werner, A simple and efficient CCSD(T)-F12 approximation, J. Chem. Phys. 127 (22) (2007).
- [50] K.A. Peterson, T.B. Adler, H.J. Werner, Systematically convergent basis sets for explicitly correlated wavefunctions: The atoms H, He, B-Ne, and Al-Ar, J. Chem. Phys. 128 (8) (2008).
- [51] K. Pfluger, M. Paulus, S. Jagiella, T. Burkert, G. Rauhut, Multi-level vibrational SCF calculations and FTIR measurements on furazan, Theor. Chem. Acc. 114 (4–5) (2005) 327–332.
- [52] B. Ziegler, G. Rauhut, Rigorous use of symmetry within the construction of multidimensional potential energy surfaces, J. Chem. Phys. 149 (16) (2018).
- [53] D. Kats, F.R. Manby, Communication: The distinguishable cluster approximation, J. Chem. Phys. 139 (2) (2013).

- [54] B. Ziegler, G. Rauhut, Efficient generation of sum-of-products representations of high-dimensional potential energy surfaces based on multimode expansions, J. Chem. Phys. 144 (11) (2016).
- [55] T. Mathea, T. Petrenko, G. Rauhut, Advances in vibrational configuration interaction theory - part 2: Fast screening of the correlation space, J. Comput. Chem. 43 (1) (2022) 6–18.
- [56] T. Mathea, G. Rauhut, Advances in vibrational configuration interaction theorypart 1: Efficient calculation of vibrational angular momentum terms, J. Comput. Chem. 42 (32) (2021) 2321–2333.
- [57] B. Schröder, G. Rauhut, Vibrational Configuration Interaction Theory, in: J. M. Bowman (Ed.), Vibrational Dynamics in Molecules, World Scientific Publishing, Singapore, 2022, pp. 1–40.
- [58] J.K.G. Watson, Simplification of molecular vibration-rotation hamiltonian, Mol. Phys. 15 (5) (1968) 479.
- [59] H.J. Werner, P.J. Knowles, F.R. Manby, J.A. Black, K. Doll, A. Hesselmann, D. Kats, A. Kohn, T. Korona, D.A. Kreplin, Q.L. Ma, T.F. Miller, A. Mitrushchenkov, K. A. Peterson, I. Polyak, G. Rauhut, M. Sibaev, The Molpro quantum chemistry package, J. Chem. Phys. 152 (14) (2020).
- [60] W.N. Lipscomb, Boron Hydrides, Dover Publications Inc, Mineola, New York, 2012.
- [61] D. Sethio, L.M.L. Daku, H. Hagemann, A theoretical study of the spectroscopic properties of B2H6 and of a series of BxHyz- species (x=1-12, y=3-14, z=0-2): From BH3 to B12H122-, Int. J. Hydrog, Energy 41 (16) (2016) 6814–6824.
- [62] P.J. Linstrom, W.G. Mallard, The NIST Chemistry WebBook: A chemical data resource on the internet, J. Chem. Eng. Data 46 (5) (2001) 1059–1063.
- [63] W.J. Lafferty, J.M. Flaud, H. Burger, G. Pawelke, The ν13, ν5+ν15 and ν9+ν15 bands of 10B2H6, J. Quant. Spectrosc. Rad. Trans. 74 (4) (2002) 445–453.
- [64] T.J. Tague, L. Andrews, Reactions of pulsed-laser evaporated boron atoms with hydrogen. Infrared spectra of boron hydride intermediate species in argon, J. Am. Chem. Soc. 116 (11) (1994) 4970–4976.
- [65] M.L. Klein, J.A. Venables, Rare Gas Solids, Academic Press, London, 1976.
- [66] J.S. Winn, Physical Chemistry, HarperCollins College Publishers, New York, 1995.
- [67] G.T. Pullen, P.R. Franke, Y.P. Lee, G.E. Douberly, Infrared spectroscopy of propene in solid para-hydrogen and helium droplets: The role of matrix shifts in the analysis of anharmonic resonances, J. Mol. Spectrosc. 354 (2018) 7–14.
- [68] T.L. Fischer, T. Wagner, H.C. Gottschalk, A. Nejad, M.A. Suhm, A rather universal vibrational resonance in 1:1 hydrates of carbonyl compounds, J. Phys. Chem. Lett. 12 (1) (2021) 138–144.
- [69] F. Bader, J.C. Tremblay, B. Paulus, Theoretical modeling of molecules in weakly interacting environments: trifluoride anions in argon, Phys. Chem. Chem. Phys. 24 (6) (2022) 3555–3567.